KD6040
Final Report
BSc (Hons) Physics

2024/2025

Tailoring the electronic properties of ZrS_2 through strain-engineering

Name: Jake Procter

ID: W21009716

Supervisor: Dr Lucy Whalley

Word Count: 10,784

Submission: 08/05/2025

Declaration

I hereby declare that the work contained in this document is all my own work. I also confirm that when this work uses ideas and opinions from the work of others, these are credited in full by citing the corresponding references.

Use of AI tool

I have used AI tools (including, but not limited to ChatGPT) to help me create bib.tex files by providing the AI with the source. I have also used AI tools to help me understand and use latex code. I have NOT used AI to generate whole sentences, paragraphs, sections, or the whole of this assignment and I understand that this would be considered academic misconduct.

Name: Jake Procter

Signature:

Jake Procter

Date: 08/05/2025

Abstract

This project investigates the influence of applied strain on the electronic properties of zirconium disulphide (ZrS_2) using density functional theory (DFT) simulations. As a quasi-2D semiconductor, ZrS_2 exhibits strain-sensitive electronic characteristics, making it a versatile material for optoelectronic and photovoltaic applications. This research aims to explore how tensile and compressive strain affect the band gap and effective mass of ZrS_2. Simulations were performed using the Atomic Simulation Environment and FHI-Aims to systematically apply in-plane and out-of-plane strain and predict the resulting electronic structure. Results indicate that tensile strain significantly reduces the band gap, with a projected semiconductor-to-metal transition at approximately -12.34% strain. In contrast, compressive strain initially increases the band gap before hybridisation effects cause a decline beyond +5% strain. Effective mass calculations reveal that tensile strain leads to a substantial increase in electron effective mass. However, compressive strain decreases the effective mass of holes. These findings demonstrate the potential for strain engineering in tuning the electronic properties of ZrS_2 for flexible electronics and next-generation semiconductor technologies. Future work includes further investigation into strain effects on charge carrier mobility and optical properties to further assess the viability of strain-engineered devices.

Contents

1 Introduction

The 21st century presents pressing global challenges, notably the dual crises of anthropogenic climate change and increasing resource scarcity. Global warming, driven by greenhouse gas emissions from fossil fuel combustion and industrial activity, has already caused a mean temperature rise of over 1.2°C above pre-industrial levels [1]. Without decisive mitigation, this trend is expected to lead to severe ecological and socioeconomic disruptions, including rising sea levels, extreme weather events, and large-scale biodiversity loss [2]. Addressing these threats requires rapidly transforming energy systems, transport infrastructure, and industrial processes, critically dependent on advanced materials. Advanced materials enable sustainable energy generation, efficient energy storage, lightweight transportation, and environmentally friendly manufacturing processes [3, 4]. Clean technologies such as solar photovoltaics, wind turbines, batteries, and hydrogen fuel cells demand materials with high efficiency, stability, and abundance. However, many materials currently used, such as cobalt for batteries or tellurium for thermoelectrics, are scarce, geographically concentrated, or environmentally problematic to extract [5, 6]. According to the International Energy Agency, demand for key transition minerals could increase sixfold by 2040 under net-zero scenarios [7]. Consequently, materials science is tasked with the dual challenge of enhancing the performance of critical technologies while discovering or engineering more sustainable alternatives.

Computational materials science, specifically density functional theory (DFT), has emerged as a cornerstone methodology for predicting, understanding, and optimising the properties of materials at the atomic scale [8, 9]. DFT allows researchers to explore new materials, investigate structure-property relationships, and propose modifications, such as doping, alloying, or mechanical strain, that can tailor material behaviour without costly experimental synthesis. Strain engineering, in particular, has gained attention as a low-carbon, reversible, and scalable approach to modify material properties, enabling fine control over electronic, optical, and mechanical characteristics without introducing chemical impurities [10, 11].

Transition metal dichalcogenides (TMDs) have occupied a central position among the diverse classes of materials explored for next-generation applications. These layered materials, characterised by the chemical formula MX_2 (M = transition metal, X = chalcogen), display a wide range of properties—from semiconducting to metallic and even superconducting behaviour—depending on their composition and structure [12, 13]. While monolayer TMD such as MoS_2, WS_2, and WSe_2 have received immense attention for their optoelectronic and valleytronic potential, the bulk forms of TMD retain technological relevance in areas like thermoelectrics, energy storage, and mechanical actuators [14, 15].

In its bulk form, ZrS_2 crystallises in the CdI_2-type layered structure with space group $P\bar{3}m1$, featuring strong in-plane Zr–S bonds and weak interlayer van der Waals interactions [16, 17]. This anisotropic bonding architecture imparts ZrS_2 with unique mechanical, electronic, and optical properties. Bulk ZrS_2 is an indirect band gap semiconductor, with DFT calculations predicting a band gap of $1.1\,eV$ to $1.7\,eV$ depending on the computational method used [18, 19]. The material demonstrates high chemical stability, environmental inertness, and mechanical flexibility, making it a compelling candidate for applications in nanoelectronics, photodetectors, flexible devices, and thermoelectrics.

Despite these promising attributes, ZrS_2 remains underexplored compared to conventional TMD like MoS_2 and WS_2. A particularly intriguing avenue is the application of mechanical strain to tailor its electronic structure. In layered materials, mechanical strain can significantly

change band dispersion, effective masses, carrier mobilities, and even induce electronic phase transitions [20, 21]. For bulk TMD, where the interlayer coupling adds another degree of complexity, strain can affect both in-plane properties and interlayer interactions, leading to novel phenomena absent in monolayer counterparts [22].

Existing studies on strain effects in bulk TMD have primarily focused on MoS_2 and WS_2. For instance, compressive strain in bulk MoS_2 has been shown to reduce the band gap and can even lead to a semiconductor-to-metal transition at high strain levels [23, 24]. Conversely, tension strain gradually reduces the band gap and modifies the effective masses, impacting carrier mobility. Similar trends have been reported for WS_2 and WSe_2 [25, 26]. These results suggest that mechanical deformation offers a robust handle to dynamically tune material properties for flexible and adaptive electronic devices.

For ZrS_2, the available literature on strain engineering remains sparse. Some computational works have investigated monolayer ZrS_2 under in-plane strain, reporting significant tunability of the band gap and effective masses [18, 17]. However, the behaviour of bulk ZrS_2 under strain, particularly along the c-axis (out-of-plane compression or tension), has not been systematically studied. Given the weak interlayer bonding in bulk ZrS_2, c-axis strain is expected to have a pronounced effect on the electronic structure by modulating interlayer distances, thereby altering the interlayer electronic coupling. Understanding these effects is crucial for device applications where bulk ZrS_2 may be subject to mechanical deformation, such as in flexible thermoelectric generators or strain-tunable electronics.

Moreover, strain engineering in bulk layered materials may offer opportunities to overcome the limitations associated with interlayer recombination and low interlayer mobility. By modulating the interlayer spacing, it may be possible to optimise charge transport pathways and thus enhance device performance. Additionally, the study of strain effects in bulk ZrS_2 could reveal emergent phenomena such as indirect-to-direct band gap transitions, enhanced carrier mobilities, or even strain-induced phase transitions—possibilities that have been theorised for other layered semiconductors but remain unverified for ZrS_2 [27, 28]. From a broader perspective, investigating the strain-dependent properties of bulk, ZrS_2 contributes to the growing field of "straintronics," where mechanical deformations are used as active control parameters for device functionality [29]. In sustainable technology development, strain engineering offers an energy-efficient and material-conserving approach to performance optimisation, aligning with global efforts to minimise resource consumption and environmental impact.

Given these motivations and knowledge gaps, this dissertation systematically investigates the effect of mechanical strain on the electronic properties of bulk ZrS_2 using first-principles DFT calculations. Particular emphasis is placed on out-of-plane strain applied perpendicular to the 2D planes, but in-plane strains are also considered to develop a comprehensive understanding. The project aims to quantify changes in the band structure, band gap, and effective carrier masses as a function of applied strain, thereby elucidating how strain modifies the electronic behaviour of bulk ZrS_2.

The computational methodology employs the all-electron code FHI-aims, with pre- and post-processing automated through the Atomic Simulation Environment (ASE) and in-house Python scripts. A range of strains, from –8% compressive to +8% tensile, is applied, leading to both linear and nonlinear deformation regimes. High k-point density and tight convergence criteria are used to ensure the accuracy of the electronic structure calculations.

This study seeks to fill a significant gap in the current materials science literature by providing a detailed map of how mechanical strain affects the key electronic properties of bulk ZrS_2. The findings are expected to inform the design of flexible and strain-adaptive devices using ZrS_2, contribute to the broader understanding of strain effects in layered semiconductors, and illustrate the value of computational approaches in sustainable materials innovation.

In conclusion, the project aligns with global sustainability goals by promoting non-invasive materials engineering, contributing to the fundamental understanding of strain–property relationships in bulk layered materials, and exemplifying the use of computational tools for accelerating materials discovery and optimisation. The research aims to advance scientific knowledge and technological sustainability in advanced materials through rigorous theoretical analysis, critical engagement with existing literature, and a focus on real-world applicability.

2 Aim and Objectives

2.1 Aim

To computationally investigate and tune the electronic properties of zirconium disulphide (ZrS_2) through strain engineering, by applying both in-plane and out-of-plane strains and analysing their effects on the electronic structure using DFT simulations.

2.2 Objectives

- Develop a foundational understanding of DFT, semiconductor theory, and the necessary processes to access and use remote supercomputers for atomistic simulations.

- Develop a reproducible computational workflow for modelling the impact of applied strain on the electronic structure of ZrS_2 using FHI-aims, the Atomic Simulation Environment (ASE), and Jupyter Notebooks (Python).

- Analyse how the electronic band gap and curvature effective mass of ZrS_2 vary with applied inter-layer and intra-layer strains, ranging from -8% to +8%.

3 Theory

3.1 Semiconductor Physics

The behaviour of charge carriers in semiconductors is crucial for predicting and tuning their electronic properties. A simplified model to describe how charge carriers respond to external forces within the crystal lattice is the effective mass. Instead of considering the interaction between each electron and the surrounding ions, the electron is treated as a free particle with an adjusted effective mass. This concept plays a central role in determining carrier mobility, a key factor in the performance of semiconductor devices.

A semiconductor is a material that can act as either a conductor or an insulator, depending on external conditions. Various factors, such as temperature, pressure, or intentional doping with impurities, can be used to modulate its electrical conductivity. The electronic band gap (Figure 1a) is the defining parameter that governs the electrical conductivity and optical absorption properties of a semiconductor.

At absolute zero temperature ($0\,\mathrm{K}$), with no external perturbations, electrons in a semiconductor are bound within the material, preventing current flow. In this state, the semiconductor behaves as an insulator. However, when external energy, such as heat or light, is applied to the material, electrons can gain sufficient energy to overcome the band gap. This allows them to move freely, leaving behind a hole in the valence band. The hole, representing the absence of an electron, also behaves as a charge carrier. This process is illustrated in Figure 1a [30].
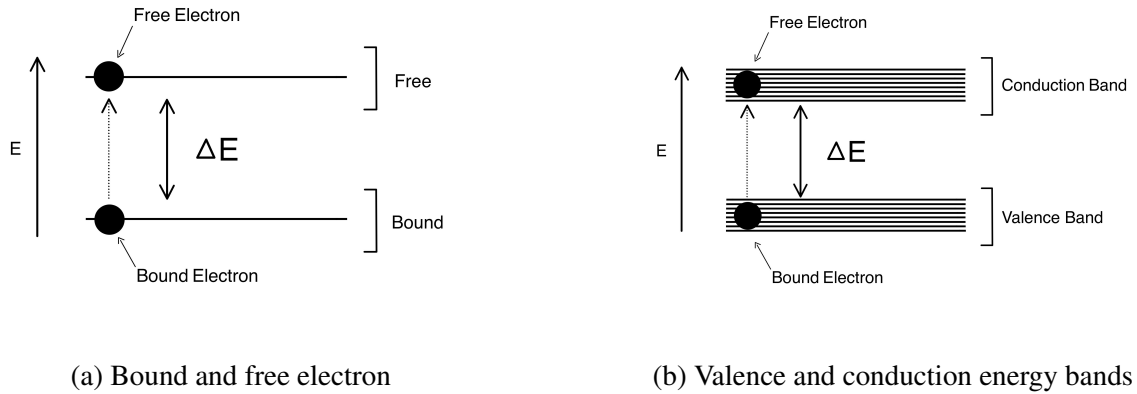

(a) Bound and free electron (b) Valence and conduction energy bands

Figure 1: Band structure diagrams illustrating the different states an electron can occupy. Subfigure 1a shows the energy gap ΔE between a bound and free electron for an isolated atom, while Subfigure 1b depicts the formation of energy bands due to multiple bonded atoms and the Pauli exclusion principle, resulting in a band gap E_g. The dashed arrow in both figures indicates the excitation process, creating an electron-hole pair.

ZrS_2 forms in a periodic crystal structure [31], and thus, the motion of an electron is influenced by the periodic potential of the crystal lattice. This interaction modifies the electron's response to external forces.

These internal forces are accounted for by the effective mass. The total force on a charge carrier is described by:

$$F_{\text{total}} = F_{\text{external}} + F_{\text{internal}} = ma, \tag{1}$$

where a is the acceleration and m is the rest mass. The internal force is written as:

$$F_{\text{internal}} = m^* a, \tag{2}$$

where m^* is the effective mass that incorporates the internal forces within the crystal structure.

The effective mass can be derived from the curvature of the electronic dispersion in reciprocal space. The expression for the curvature effective mass m_c is:

$$\frac{1}{m_c} = \frac{1}{\hbar^2} \frac{d^2 E}{dk^2} \tag{3}$$

This relationship, known as the curvature effective mass, is inversely proportional to the second derivative of the energy with respect to the wavevector k, as illustrated in Figure 2.

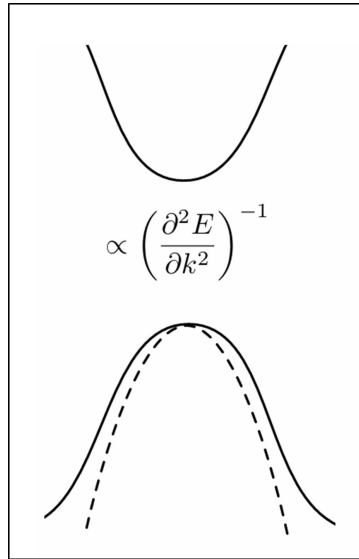Figure 2: Schematic of curvature effective mass. The effective mass is inversely proportional to the curvature of the electronic band structure of a material. Adapted from [32].

The effective mass is a critical parameter in determining the transport properties of semiconductors, as it directly affects carrier mobility. The relationship between mobility μ and effective mass is given by:

$$\mu = \frac{q\tau}{m^*}, \tag{4}$$

where q is the charge of the carrier, τ is the mean scattering time, and m^* is the effective mass. This expression shows that mobility is inversely proportional to effective mass: lower effective mass results in higher mobility. This is particularly important in photovoltaic (PV) applications, where carrier mobility affects performance metrics such as short-circuit current. In two-dimensional materials, the effective mass is often anisotropic due to reduced symmetry and quantum confinement, leading to direction-dependent mobility variations. Therefore, understanding how effective mass varies with strain and crystallographic direction is crucial for optimising device performance.

3.2 Density Functional Theory

DFT is a highly effective and popular technique used for computational modelling of materials from first principles [33]. When modelling a complex many-atom system, there are many possible atom-atom, electron-electron and atom-electron interactions. DFT solves approximate versions of the Schrödinger equation to provide insights into these systems. This project aims to understand how strain can be used to control the electronic properties of ZrS_2 by analysing how the electronic band gap and effective mass vary with an applied strain. Therefore, DFT calculations will be used to calculate the electronic band energies $E(k)$ where k is the crystal momentum in reciprocal space (see Section 3.2.7). The mathematical concepts covered in this section are derived from chapters 2 and 3 of reference [33].

3.2.1 The Schrödinger equation

To understand the behaviour of quantum particles, we need to determine the wavefunction $\psi(\mathbf{r})$ for every point of interest by solving the Schrödinger equation. For stationary electronic states, we use the time-independent Schrödinger equation:

$$-\frac{\hbar^2}{2m}\frac{d^2\psi(\mathbf{r})}{dx^2} + V(\mathbf{r})\psi(\mathbf{r}) = E\psi(\mathbf{r}), \tag{5}$$

where $\psi(\mathbf{r})$ is the wavefunction, E is the energy eigenvalue, $V(\mathbf{r})$ is the potential energy function, $\hbar$ is the reduced Planck's constant, and m is the mass of the particle. The probability of finding a particle at point $\mathbf{r}$ is given by $|\psi(\mathbf{r})|^2$.

More formally, we can express the same equation using operator notation:

$$\left(\hat{T} + \hat{V}\right)\psi = E\psi, \tag{6}$$

where $\hat{T}$ and $\hat{V}$ are the kinetic and potential energy operators, respectively.

3.2.2 The many-body Schrödinger equation

For many-electron and nuclei systems, we introduce a many-body wavefunction, Ψ, which depends on the positions of each electron and each nucleus in the system. Therefore, the time-independent Schrödinger equation becomes:

$$\left(\hat{T} + \hat{V}\right)\Psi = E\Psi, \tag{7}$$

The kinetic energy now has to take into account N electrons and M nuclei:

$$\text{Kinetic energy} = -\sum_{i=1}^{N} \frac{\hbar^2}{2m_e} \nabla_i^2 - \sum_{I=1}^{M} \frac{\hbar^2}{2M_I} \nabla_I^2, \tag{8}$$

where m_e is the electron mass, M_I are the masses of the nuclei, the index i runs over the electrons, and the index I runs over the nuclei.

The potential energies are attained through Coulomb interactions derived from electrostatic Coulomb equations. First, the Coulomb repulsion between electron pairs:

$$(\text{Potential energy})_{ee} = \frac{1}{2} \sum_{\substack{i,j=1 \\ i \neq j}}^{N} \frac{e^2}{4\pi\epsilon_0} \frac{1}{|\mathbf{r}_i - \mathbf{r}_j|}, \tag{9}$$

where the indices i and j run over all N electrons, and terms with $i = j$ are excluded because an electron does not repel itself. Secondly, the Coulomb repulsion between nuclei pairs:

$$(\text{Potential energy})_{nn} = \frac{1}{2} \sum_{\substack{I,J=1 \\ I \neq J}}^{M} \frac{e^2}{4\pi\epsilon_0} \frac{Z_I Z_J}{|\mathbf{R}_I - \mathbf{R}_J|}, \tag{10}$$

where I and J run over all M nuclei, and Z_I and Z_J are the atomic numbers of the respective nuclei. Finally, the Coulomb attraction between electrons and nuclei:

$$(\text{Potential energy})_{en} = -\sum_{i=1}^{N} \sum_{I=1}^{M} \frac{e^2}{4\pi\epsilon_0} \frac{Z_I}{|\mathbf{r}_i - \mathbf{R}_I|}, \tag{11}$$

with i running over electrons and I over nuclei [34].

As we now have all the necessary components, the many-body Schrödinger equation can be written [35]:

$$\left[-\sum_{i=1}^{N} \frac{\hbar^2}{2m_e} \nabla_i^2 - \sum_{I=1}^{M} \frac{\hbar^2}{2M_I} \nabla_I^2 + \frac{1}{2} \sum_{\substack{i,j=1 \\ i \neq j}}^{N} \frac{e^2}{4\pi\epsilon_0} \frac{1}{|\mathbf{r}_i - \mathbf{r}_j|} \right.$$
$$\left. + \frac{1}{2} \sum_{\substack{I,J=1 \\ I \neq J}}^{M} \frac{e^2}{4\pi\epsilon_0} \frac{Z_I Z_J}{|\mathbf{R}_I - \mathbf{R}_J|} - \sum_{i=1}^{N} \sum_{I=1}^{M} \frac{e^2}{4\pi\epsilon_0} \frac{Z_I}{|\mathbf{r}_i - \mathbf{R}_I|} \right] \Psi = E_{\text{Total}} \Psi, \tag{12}$$

where Ψ is the many-body wavefunction depending on all electron and nuclear coordinates, and E_{Total} is the total energy of the system.

The many-body Schrödinger equation contains almost everything needed to study the behaviour of materials at equilibrium. When this equation is solved, and the eigenstate with the lowest energy is found, i.e., the system's ground state, calculations can be carried out to predict many properties of the material. However, even for the smallest systems (a few molecules), solving this equation exactly is practically impossible due to the enormous number of variables involved. Consequently, approximations to the many-body Schrödinger equation are essential in materials modelling to make these complex calculations tractable.

3.2.3 Approximations of the many-body Schrödinger equation

The first step in approximating equation (12) is estimating the magnitude of the kinetic energies in the system. This is done from the Hartree energy:

$$E_{Ha} = \frac{e^2}{4\pi\epsilon_0 a_0}. \tag{13}$$

E_{Ha} is defined as the average Coulomb energy for an electron-proton pair [36]. It is also the Coulomb energy for a pair of two protons or a pair of electrons at the same distance. After balancing the centrifugal force and the nuclear attraction, we arrive at a useful relation:

$$\frac{1}{2}m_e v_2 = \frac{1}{2}E_{Ha}. \tag{14}$$

This relation leads us to adjust our initial many-body Schrödinger equation (12) using the Hartree energy to attain [35]:

$$\left[-\sum_{i=1} \frac{\nabla_i^2}{2} - \sum_{i=1} \frac{\nabla_i^2}{2M_I} - \sum_{i,I} \frac{Z_I}{|\mathbf{r}_i - \mathbf{R}_I|} + \frac{1}{2}\sum_{i\neq j} \frac{1}{|\mathbf{r}_i - \mathbf{r}_j|} + \frac{1}{2}\sum_{I\neq J} \frac{Z_I Z_J}{|\mathbf{R}_I - \mathbf{R}_J|} \right]\Psi = E_{Total}\Psi. \tag{15}$$

This is the most common form of the many-body Schrödinger equation used in materials modelling, however, this is too general for crystal structures as it describes almost everything, from solids to gases. The nuclei in crystal structures like ZrS_2 are nearly immobile; therefore, it is intuitive to think of their mass as so great that they cannot move. Consequently, we can set $M_1 = \infty$, and neglect the kinetic energy so the Coulomb repulsion between nuclei becomes a constant [33]:

$$E = E_{\text{Total}} \underbrace{-\frac{1}{2}\sum_{I\neq J} \frac{Z_I Z_J}{|\mathbf{R}_I - \mathbf{R}_J|}}_{Constant}. \tag{16}$$

As such:

$$\left[-\sum_{i=1} \frac{\nabla_i^2}{2} - \sum_{i,I} \frac{Z_I}{|\mathbf{r}_i - \mathbf{R}_I|} + \frac{1}{2}\sum_{i\neq j} \frac{1}{|\mathbf{r}_i - \mathbf{r}_j|} \right]\Psi = E_{Total}\Psi. \tag{17}$$

We can further reduce this equation by defining the *Coulomb potential of the nuclei experienced by the electrons* [33]:

$$V_n(\mathbf{r}) = -\sum_I \frac{Z_I}{|\mathbf{r} - \mathbf{R}_I|} \tag{18}$$

so the nuclear coordinates disappear:

$$\left[-\sum_{i=1} \frac{\nabla_i^2}{2} - \sum_i V_n(\mathbf{r}_i) + \frac{1}{2} \sum_{i \neq j} \frac{1}{|\mathbf{r}_i - \mathbf{r}_j|} \right] \Psi = E_{Total} \Psi. \tag{19}$$

This is the *fundamental equation of electronic structure theory* [33]. We can simplify this equation further by introducing the many-electron Hamiltonian:

$$\hat{H}(\mathbf{r}_1, \mathbf{r}_2..., \mathbf{r}_N) = -\sum_i \frac{1}{2} \nabla_i^2 + \sum_i V_n(\mathbf{r}_i) + \frac{1}{2} \sum_{i \neq j} \frac{1}{|\mathbf{r}_i - \mathbf{r}_j|} \tag{20}$$

.

Therefore:

$$\hat{H} \Psi = E \Psi \tag{21}$$

3.2.4 The Hohenberg-Kohn theorem

At its core, DFT states that if E is the energy of the ground state of the system, then E is a functional of the electron density only [35]:

$$E = F[n]. \tag{22}$$

This observation is due to Hohenberg and Kohn [37] and shows all that is needed for calculating the total energy, E, for the ground state is the electron density, n.

3.2.5 The Kohn-Sham equations

DFT and FHI-aims, which we will discuss later, utilise the Kohn–Sham equations that arise from the abovementioned equations. References [33, 35, 38] provide further context and mathematical derivations of these equations.

An iterative process called a self-consistent field (SCF) cycle determines the electron density. An approximate electron density is initially obtained by summing the densities of isolated atoms positioned according to the material's structure [39]. From this initial guess, an estimate of the system's total potential is derived, enabling the numerical solution of the Kohn–Sham equations.
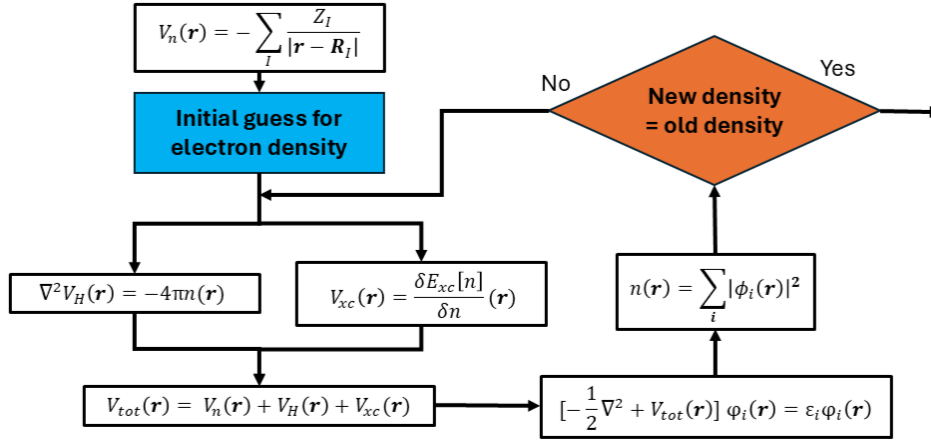

Figure 3: Flowchart illustrating the procedure for obtaining self-consistent solutions of the Kohn–Sham equations, adapted from a presentation in Reference [40].

The flowchart presented in Figure 3 outlines the iterative procedure for finding self-consistent solutions to the Kohn–Sham equations. The process begins with calculating the external potential $V_n(\mathbf{r})$, previously discussed (Equation 18):

$$V_n(\mathbf{r}) = -\sum_I \frac{Z_I}{|\mathbf{r} - \mathbf{R}_I|}$$

Next, the Hartree potential $V_H(\mathbf{r})$ is obtained by solving the Poisson equation, accounting for electron-electron Coulomb interactions:

$$\nabla^2 V_H(\mathbf{r}) = -4\pi n(\mathbf{r}) \tag{23}$$

The exchange-correlation potential $V_{xc}(\mathbf{r})$ is computed as the functional derivative of the exchange-correlation energy:

$$V_{xc}(\mathbf{r}) = \frac{\delta E_{xc}[n]}{\delta n(\mathbf{r})} \tag{24}$$

These potentials are combined to form the total effective potential:

$$V_{tot}(\mathbf{r}) = V_n(\mathbf{r}) + V_H(\mathbf{r}) + V_{xc}(\mathbf{r}) \tag{25}$$

Using this effective potential, the Kohn–Sham equations are solved to obtain single-particle wavefunctions $\phi_i(\mathbf{r})$ and their corresponding energies ϵ_i:

$$\left[-\frac{1}{2}\nabla^2 + V_{tot}(\mathbf{r})\right]\phi_i(\mathbf{r}) = \epsilon_i\phi_i(\mathbf{r}) \tag{26}$$

The electron density is updated as:

$$n(\mathbf{r}) = \sum_i |\phi_i(\mathbf{r})|^2 \tag{27}$$

This procedure iterates with each cycle, updating the potential and wavefunctions until convergence. Due to the complexity of these calculations, high-performance computing resources are required [35].

3.2.6   DFT functionals

DFT functionals are mathematical approximations that describe electron exchange and correlation effects in quantum mechanical systems. These functionals are essential for accurately capturing the complex interactions between electrons within materials. DFT functionals are classified into local, semi-local, hybrid, and double-hybrid types [38], each offering a balance between computational cost and accuracy.
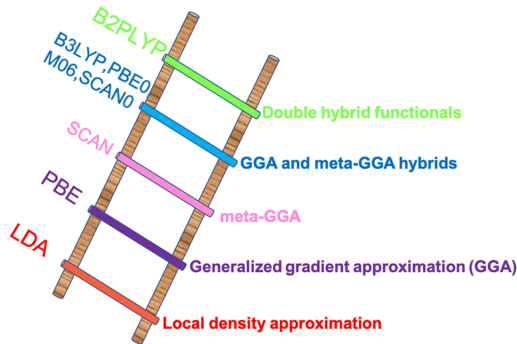

Figure 4: Jacob's ladder for exchange-correlation functionals in DFT, reproduced from Reference [41]. The figure illustrates the hierarchical structure of functionals.

The concept of Jacob's ladder in DFT, depicted in Figure 4, metaphorically illustrates the hierarchy of DFT functionals. Each rung represents an improvement in accuracy at the expense of increased computational effort.

Local functionals at the ladder's base, such as the Local Density Approximation (LDA) [42], which consider only the electron density at a given point. The next rung consists of semi-local functionals, including Generalised Gradient Approximation (GGA) [43] methods like PBE

[44], which incorporate the gradient of the electron density to improve accuracy. Hybrid functionals, such as HSE [45], lie higher on the ladder, combining a fraction of exact Hartree–Fock exchange with GGA, enhancing the description of electronic interactions. Double-hybrid functionals, at the top, further include non-local correlation effects, but they are computationally demanding.

Choosing the appropriate functional for the desired calculations is crucial in materials modelling, as each functional exhibits strengths and weaknesses depending on the property being investigated, such as reaction energies or band gaps. Details on the two functionals used in this study are outlined below.

PBE

The Perdew-Burke-Ernzerhof (PBE) functional [43] is a generalised gradient approximation (GGA) developed in 1996 to improve the accuracy of DFT calculations. It modifies earlier approximations like the Becke-88 [46] and PW91 [47] functionals by introducing a gradient correction to account for the inhomogeneity of the electron density. The PBE function provides a more accurate description of exchange-correlation energies, especially for systems with a varied electron density. The mathematical formulation of PBE presented here is sourced from [43].

The exchange-correlation energy in PBE is given by an integral over space:

$$E_{xc}^{\text{PBE}} = \int \epsilon_{xc}^{\text{PBE}}(n(\mathbf{r}), \nabla n(\mathbf{r})) \, d^3r \tag{28}$$

where $\epsilon_{xc}^{\text{PBE}}$ is the exchange-correlation energy density, which depends on both the electron density $n(\mathbf{r})$ and the gradient of the density $\nabla n(\mathbf{r})$.

The exchange energy part of the functional is written as:

$$E_x^{\text{PBE}} = \int n(\mathbf{r}) \epsilon_x^{\text{PBE}}(n(\mathbf{r}), s) \, d^3r \tag{29}$$

where $s = \frac{|\nabla n|}{2k_F n}$ is the reduced density gradient, and k_F is the Fermi wave vector. This formulation ensures the function satisfies important physical constraints such as correct scaling behaviour and the Lieb-Oxford bound.

Similarly, the correlation energy is given by:

$$E_c^{\text{PBE}} = \int n(\mathbf{r}) \epsilon_c^{\text{PBE}}(n(\mathbf{r}), \nabla n(\mathbf{r})) \, d^3r \tag{30}$$

where ϵ_c^{PBE} represents the correlation energy density. This term is based on the spin-polarised LDA correlation but includes a correction to account for the electron density gradient.

The PBE functional has become one of the most widely used functionals in DFT due to its balance between computational efficiency and accuracy. It is particularly well-suited for predicting the structural and energetic properties of solids and molecular systems. However, like all GGAs, PBE has limitations, including the underestimation of band gaps in semiconductors by approximately 40% and the poor treatment of dispersion interactions without additional corrections, as reported in a comprehensive study evaluating various exchange-correlation functionals, including PBE [48].

HSE06

The Heyd-Scuseria-Ernzerhof (HSE) functional is a hybrid exchange-correlation functional developed to improve the accuracy of DFT calculations, especially for electronic structure and band gap predictions. HSE06, a specific variant of the HSE functional, introduces a portion of exact exchange into the generalised gradient approximation (GGA) framework [49]. This combination provides a more accurate description of electronic interactions, particularly in systems where the description of band gaps is essential.

The HSE function is based on a fraction of the exact Hartree-Fock exchange, combined with the PBE GGA for the correlation and the remaining exchange contributions. The following expression gives the exchange-correlation energy in HSE06:

$$E_{xc}^{\text{HSE06}} = E_x^{\text{HSE06}} + E_c^{\text{PBE}}, \tag{31}$$

where E_x^{HSE06} represents the exchange energy and E_c^{PBE} is the correlation energy from the PBE functional. The exchange energy in HSE06 is a hybrid functional, meaning that part of the exchange comes from the exact Hartree-Fock exchange, E_x^{HF}, and part from a GGA functional like PBE. The exchange energy is written as:

$$E_x^{\text{HSE06}} = (1 - \alpha)E_x^{\text{PBE}} + \alpha E_x^{\text{HF}}, \tag{32}$$

where α is the mixing parameter, which in HSE06 is typically set to 0.25 [49]. This parameter controls the fraction of exact exchange mixed with the GGA exchange energy. The parameter E_x^{HF} represents the Hartree-Fock exchange, which accounts for the long-range behaviour of electron-electron interactions more accurately than pure DFT functionals.

The correlation energy E_c^{PBE} in HSE06 is still based on the PBE functional, which uses the local density and gradient corrections, but with the exchange component modified as described above. The correlation part does not include exact exchange but retains the GGA correction to account for electron-electron interactions.

The HSE06 functional is particularly effective in correcting the underestimation of band gaps in semiconductors and insulators, as demonstrated in the findings of the study [48], which is a common issue with pure GGA functionals like PBE, as previously discussed. By incorporating exact exchange, the HSE06 functional offers a more accurate description of the electronic structure, particularly for materials with significant electronic correlation effects. However, like all hybrid functionals, HSE06 requires a higher computational cost due to the inclusion of exact exchange, making it more demanding than pure GGA functionals.

3.2.7 K-Point sampling

In periodic systems, such as crystal structures, the first Brillouin zone is the region of reciprocal space that contains all unique wave vectors necessary to describe the system's electronic structure. The first Brillouin zone is equivalent to the Wigner-Seitz unit cell of the reciprocal lattice. Directly solving the Kohn-Sham equations at every point in the Brillouin zone is computationally impractical. Instead of considering all possible k-points in the continuous Brillouin zone, a discrete set of k-points is chosen to efficiently approximate the electronic properties. The selection of these k-points, including their number and distribution, plays a crucial role in both the accuracy and computational cost of the calculation. A higher density of k-points improves accuracy but increases the computational time, while a sparser set reduces the cost but may sacrifice precision.
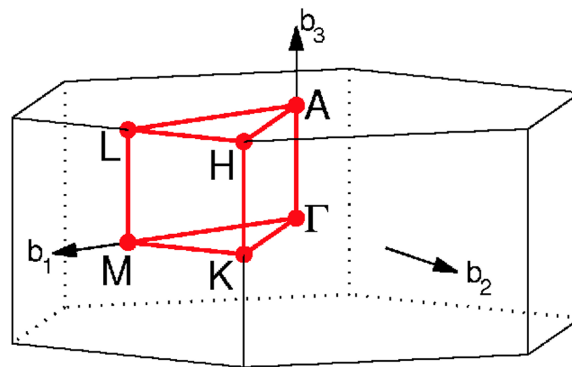

Figure 5: Brillouin zone for ZrS_2, which has a hexagonal lattice structure. The figure shows the first Brillouin zone and its symmetry. Reproduced from Figure 13 in [50].

As illustrated in Figure 5, the Brillouin zone for ZrS_2 is hexagonal in shape, reflecting the material's hexagonal crystal structure. It is important to note that the size of the Wigner-Seitz cell in real space inversely affects the size of the corresponding Brillouin zone. A larger cell in real space results in a smaller Brillouin zone and thus requires a more finely spaced selection of k-points for accurate simulations.

A sparse k-point sampling (large k-spacing) employs fewer k-points, reducing the computational cost. While suitable for large supercells and preliminary studies, it may lead to errors in band structure and total energy calculations. An intermediate k-point sampling provides a balanced approach, ensuring reasonable accuracy without excessive computational demands. It is commonly used in standard materials simulations. Finally, a dense k-point sampling (small k-spacing) ensures high precision but significantly increases computational cost.

Selecting an appropriate k-point spacing requires a trade-off between accuracy and efficiency, with convergence testing used to determine the optimal sampling density.

4 Methodology

All DFT calculations in this study were performed using remote high-performance computing (HPC) infrastructure. Access was achieved through Secure Shell (SSH) protocols within a Linux command-line environment, providing an efficient platform for submitting jobs, managing files, and interacting with computational resources. File transfers between local and remote machines were routinely carried out using the secure copy protocol (SCP). To ensure full reproducibility and transparency of the computational workflow, all Python scripts for preprocessing, post-processing, and automation were version-controlled and made publicly available through a dedicated GitHub repository [51].

4.1 Structure preparation and preprocessing

The initial crystal structure of ZrS_2 was sourced from the Materials Project database [52], a widely trusted platform offering experimentally validated crystallographic data. Structures were parsed, visualised, and manipulated using the Atomic Simulation Environment (ASE) Python package [53], which facilitated the modification of lattice parameters and atomic positions in a consistent and reproducible manner.

Strain refers to the deformation of a material resulting from applied stress and is defined mathematically as:

$$\varepsilon = \frac{a - a_0}{a_0} \times 100\% \tag{33}$$

where a_0 and a are the unstrained and strained lattice constants. Strain can be tensile ($\varepsilon < 0$), associated with stretching and increasing lattice parameters, or compressive ($\varepsilon > 0$), corresponding to compression and reduced lattice constants. In two-dimensional materials such as ZrS_2, strain can be applied either out-of-plane (along a single crystallographic direction) or in-plane (simultaneously along two directions).

A custom Python script was developed to implement strain that systematically altered the lattice vectors. Two simulations were prepared: out-of-plane strain along the c-axis and in-plane strain along the a- and b-axes, as illustrated in Figure 6, where the top view shows the a- and b-axes and the side view shows the c-axis. Strain levels ranged from -8% to +8% in integer increments, allowing for a detailed study of electronic structure evolution.
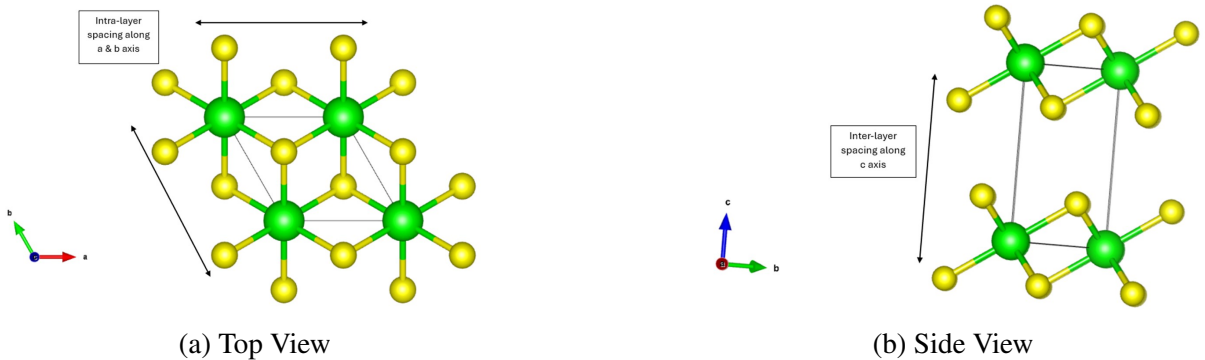

(a) Top View

(b) Side View

Figure 6: ZrS2 Crystal Structure

The ASE package was employed to scale the lattice while carefully preserving the internal atomic positions, minimising structural artefacts and enabling reliable comparisons between strained configurations.

The stability of strained structures was assessed by calculating the strain energy, which is defined as the difference in total DFT energy between the strained and unstrained systems. Within moderate strain regimes, strain energy typically exhibits a quadratic dependence on strain magnitude, indicating elastic behaviour [54]. Importantly, it is noted that in-plane strain generally results in higher strain energies than out-of-plane strain, reflecting the increased energetic cost of uniform deformation along multiple axes.

4.2 Convergence testing

Thorough convergence testing was performed before production simulations to determine appropriate values for numerical parameters, ensuring a balance between computational cost and accuracy.

Convergence tests targeted three primary variables:

- DFT Functional: The PBE [44] and HSE06 [45] functionals were tested to compare their accuracy and computational time differences, ultimately determining the most suitable functional for the study.

- K-point density: Sampling of the Brillouin zone was performed using k-point grids ranging from 2×2×2 to 14×14×14 in increments of 2, in order to optimise the trade-off between accuracy and computational cost.

- Basis set size: Simulations using FHI-aims' predefined "light", "intermediate", and "tight" basis sets were compared to gauge basis set sensitivity.

All convergence results were carefully documented and used to standardise parameters across all simulations, ensuring consistency.

4.3 Simulation workflow

All DFT simulations were conducted using the FHI-aims electronic structure code [38], selected for its all-electron formalism and demonstrated reliability for 2D materials studies. Bash scripts were created to automate job submission, file handling, and resource management on the HPC cluster. Simulations were parallelised using the Message Passing Interface (MPI) to optimise computational efficiency.

4.4 Post-processing and data analysis

After completion, all simulation output files were securely transferred back to local storage using SCP for analysis. The electronic properties of each configuration were extracted through a combination of manual inspection and scripted automation.

Band structures were processed using a series of custom Python functions. The electronic band gap was determined by calculating the energy difference between the highest occupied molecular orbital (HOMO) and the lowest unoccupied molecular orbital (LUMO) as reported in each `aims.out` file.

As discussed in Section 3.1, the curvature effective mass of charge carriers was determined using the second derivative of the energy-momentum ($E(k)$) relation. Here is equation 3 rearranged for m^*:

$$m^* = m_c = \hbar^2 \left(\frac{d^2 E}{dk^2} \right)^{-1} \tag{34}$$

Band structures were fitted with second-order polynomials near the conduction and valence band extrema to compute the second derivatives. The `effmass` Python package [55] was used to automate this process, which employs a least-squares fit to calculate the effective masses. This approach provided reproducible and statistically robust estimates of effective masses, ensuring reliable and consistent results.

In this study, the carrier mobility (μ) was calculated using the deformation potential theory [56], which attributes scattering primarily to acoustic phonons. This method has been widely applied to 2D materials and yields insight into intrinsic transport properties. The mobility is given by:

$$\mu = \frac{2e\hbar^3 C}{3k_B T (m^*)^2 E_{\text{def}}^2} \tag{35}$$

where:

- $e = 1.602 \times 10^{-19}\,\text{C}$ is the elementary charge,

- $\hbar = 1.055 \times 10^{-34}\,\text{J s}$ is the reduced Planck constant,

- $C = 130\,\text{GPa}$ in-plane & $C = 30\,\text{GPa}$ out-of-plane elastic modulus of ZrS_2 [57],

- $k_B = 1.381 \times 10^{-23}\,\text{J K}^{-1}$ is the Boltzmann constant,

- $T = 300\,\text{K}$ is the temperature,

- m^* is the effective mass of the charge carrier (in units of the free electron mass m_0),

- $E_{\text{def}} = 5.0\,\text{eV}$ is the deformation potential constant [58].

As this equation reveals, carrier mobility is inversely proportional to the square of the effective mass, and this trend is reflected clearly in Figure 20. The deformation potential E_{def} quantifies the shift in band edge energy for strain and is a key parameter in determining mobility. A value of $5.0\,\text{eV}$ was selected based on precedent in related materials, such as monolayer MoS_2, where deformation potentials typically lie between $4\,\text{eV}$ and $6\,\text{eV}$ [58]. Given its use in similar studies of 2D semiconductors, this theoretical framework was deemed appropriate for ZrS_2.

The elastic modulus along the c-axis was obtained from DFT-based stress-strain calculations and is consistent with reported values for layered materials, where the weak van der Waals interlayer bonding results in relatively low out-of-plane stiffness [59]. Specifically, the c-axis elastic modulus of ZrS_2 was extracted from the calculations of Zhao et al. [57], who reported it to be approximately $30\,\text{GPa}$. Similarly, the in-plane modulus along the a–b plane was derived from the same study and was found to be approximately $130\,\text{GPa}$. These parameters were used to estimate carrier mobility following the deformation potential theory as originally formulated by Bardeen and Shockley [60].

A Python script was used to automate the mobility calculations. Using the effective masses derived from DFT via the `effmass` package, the script applied Equation 35 to each data point and generated a complete set of mobilities for electrons and holes under varying strain conditions.

Data visualisation was performed using `matplotlib` [61]. Graphs illustrating the band structures under varying strains and plots tracking the band gap and effective masses as functions of strain were generated. To enhance interpretation, an animated GIF was created to illustrate the evolution of the band structure across the full range of strain values. The GIF can be found in the GitHub repository [51].

4.5 Uncertainty and limitations

Despite rigorous convergence testing, several sources of uncertainty and limitations must be acknowledged. One of the primary limitations arises from the functional choice. Although the PBE functional is computationally less intensive and widely used for studies of electronic properties, it tends to underestimate the absolute band gap. This is evident in Figure 8, where the calculated band gap converges between $1\,\text{eV}$ and $1.05\,\text{eV}$. This represents a significant underestimation compared to previous calculations by [62], which reported a band gap of $1.98\,\text{eV}$. The observation of the band gap under strain is a key objective of this study. Therefore, the more accurate Heyd-Scuseria-Ernzerhof (HSE06) hybrid functional was selected for its superior performance in predicting band gaps. Although HSE06 comes with a significantly higher computational cost, its use was justified by the need for accurate band gap determination. As illustrated in Figure 7, a single unstrained ZrS_2 calculation using HSE06 (tight, 14×14×14) required 1619 seconds, compared to just 31 seconds for PBE under the same conditions. Using HSE06 ensures more reliable band gap predictions, where a converged band gap of $1.83\,\text{eV}$ was observed. This is crucial for understanding the strain effects on ZrS_2, although it comes at the cost of significantly increased computational resources.
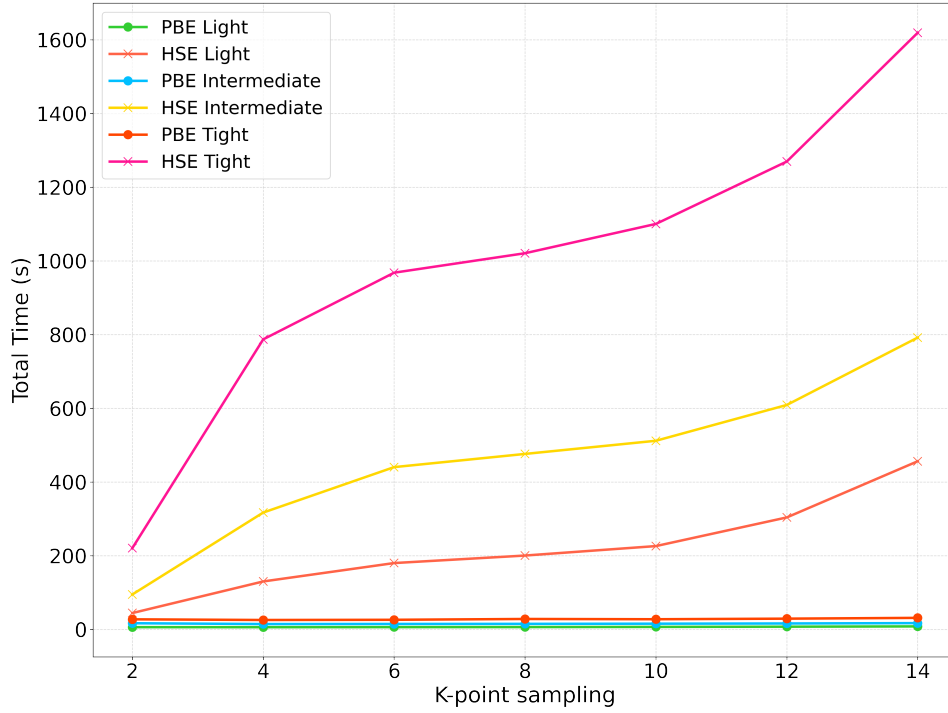

Figure 7: Total time as a function of k-point sampling mesh. The sampling mesh is the same in all directions; for example, 8 indicates a 8x8x8 grid in reciprocal space. for PBE and HSE

Another limitation is that DFT, including both the PBE and HSE06 functionals, does not explicitly account for van der Waals (VDW) interactions. This omission can be significant in systems with weakly interacting components, such as layered 2D materials like ZrS_2. While this lack of VDW interaction consideration may impact structural parameters, it is expected to have minimal effect on the band gap evolution under strain, which is the primary focus of this study [63].

Additionally, spin effects were neglected in the calculations, assuming the system remains non-magnetic under all strain conditions. This is a common simplification in studies of non-magnetic 2D materials, where spin-polarised effects are typically insignificant for the band gap analysis [64]. However, this assumption may limit the accuracy of the results in systems where spin-polarised effects could play a role, though this is not anticipated to be a significant factor in the case of ZrS_2.

The extraction of effective masses involves fitting band structures with second-order polynomials, and the fitting process itself can introduce minor errors, especially if the band extrema are broad or asymmetric. These errors are generally small, but they must be considered when interpreting the results.

The extraction of effective masses involves fitting band structures with second-order polynomials using a least squares fit, and the fitting process itself can introduce minor errors, especially if the band extrema are broad or asymmetric. These errors are generally minor but must be considered when interpreting the results. Ideally, convergence testing for various fit parameters, such as the range of data points and the polynomial order, would be conducted to ensure the accuracy of the extracted effective masses. However, this additional work was not feasible due to time constraints during this research. Consequently, the results presented here are based on the least squares fitting procedure without full convergence testing.

Furthermore, the study applies strain in integer per cent steps, which may not capture subtle transitions that could occur between sampled points. Using smaller strain increments could provide a more detailed picture of the band gap evolution, but this was not feasible within the scope of this study.

Lastly, the material's elastic limit was set at $\pm 8\%$, as larger strains may lead to structural instabilities or phase transitions that were not captured in this work. Thus, while the strain range explored provides valuable insights, it is limited to moderate strain values, and larger deformations could yield different results not represented in this study.

In summary, while these limitations are uncertain, they have been carefully considered during result interpretation. The methodology employed provides a solid and reproducible foundation for understanding the effects of strain on the electronic properties of ZrS_2, despite these inherent challenges.

All input files, scripts, raw data, and visualisations are publicly available in the dedicated GitHub repository [51] to facilitate independent verification and further research.

5 Results and discussion

5.1 Convergence tests

To ensure the accuracy and efficiency of the DFT simulations, convergence tests were conducted on the k-point mesh, exchange-correlation functional, and basis set. These tests determined the optimal computational parameters for reliable electronic structure calculations under applied strain.

A k-point mesh defines the grid of sampling points in reciprocal space used to approximate the electronic band structure. Sampling of the Brillouin zone was performed using k-point grids ranging from 2×2×2 to 14×14×14 in increments of 2. The results showed that below 8×8×8, the total energy and band gap fluctuated significantly, indicating insufficient sampling. At 14×14×14, the band gap had converged, as seen by the reduction in band gap value differences in Figure 8 and Figure 9, confirming that this grid balanced accuracy and computational cost. For this reason, 14×14×14 was chosen as the k-point mesh for all calculations.

Two functionals were tested: the Perdew-Burke-Ernzerhof (PBE) functional, as shown in Figure 8, and the hybrid Heyd-Scuseria-Ernzerhof (HSE06) functional, as shown in Figure 9.

PBE consistently underestimated the band gap, as expected (see section 3.2.6) for generalised gradient approximation (GGA) functionals. HSE06 produced more accurate band gaps but required significantly longer computational times. Despite the increased cost, HSE06 was selected for all strain-dependent calculations due to its superior predictive accuracy.
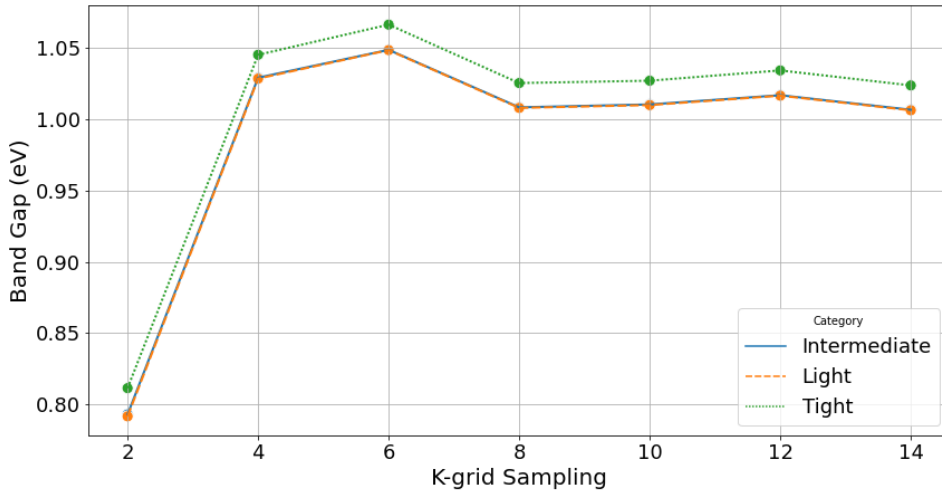

Figure 8: PBE band gap vs k-grid

The basis set convergence was evaluated using light, intermediate, and tight settings in FHI-Aims. The tight basis provided the most accurate band gap values but at a higher computational expense. Given its precision, the tight basis was chosen for the final simulations.
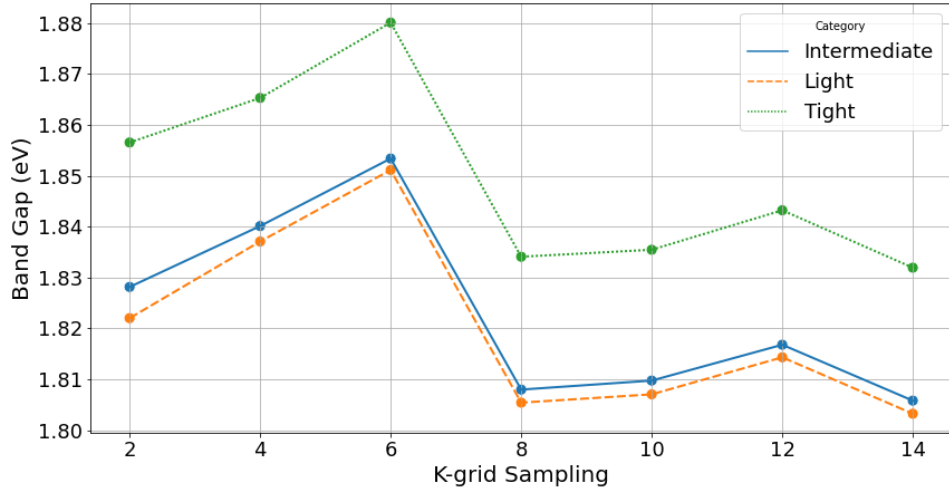
Figure 9: HSE06 band gap vs k-grid

These convergence tests established that the **HSE06 functional, 14×14×14 k-grid, and tight basis set** provided the most reliable and computationally efficient setup for modelling the electronic properties of ZrS_2 under strain.

5.2 ZrS₂ with zero applied strain

To validate our computational approach, we first compare the electronic structure of ZrS$_2$ with zero applied strain against previously published research (Figure 10).
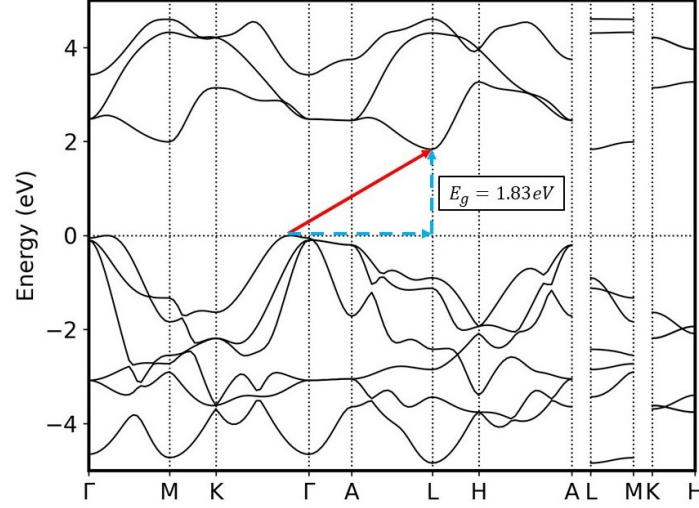

Figure 10: Band structure plot of ZrS$_2$ under zero applied strain

Figure 10 shows the band structure plot of ZrS$_2$ with zero applied strain. The experimentally determined band gap of ZrS$_2$ is indirect and falls within the range $1.78\,\text{eV}$ - $1.86\,\text{eV}$ [65]. We observe an indirect band gap of $1.83\,\text{eV}$, which is in line with the experimental reports. Computational predictions have previously estimated a band gap as high as $1.94\,\text{eV}$ [62]. Our improved prediction likely results from the choice of functional and the inclusion of a more accurate treatment of electron-electron interactions, such as the hybrid functional used in this study. This difference highlights the importance of incorporating more sophisticated exchange-correlation functionals to achieve better agreement with experimental data.
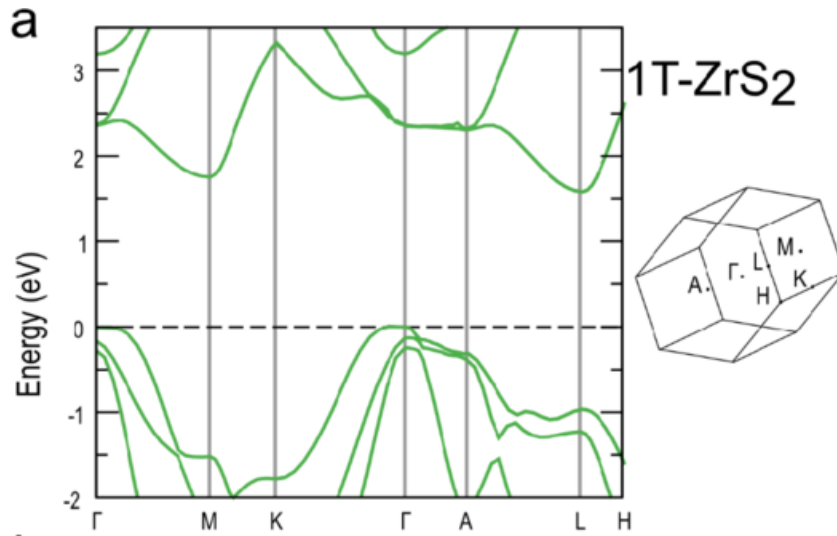

Figure 11: Band structure plot of ZrS$_2$ taken from Figure 4a from [66].

Figure 10 shows that the valence band maximum (VBM) lies slightly off the Γ point, while the conduction band minimum (CBM) is located at the L point in the Brillouin zone. This

indirect nature of the band gap suggests weaker optical absorption at the band edge and limited efficiency for radiative recombination, consistent with the electronic behaviour of many layered TMDs [67].

Figure 11 presents a previously published band dispersion for ZrS_2 derived from DFT with the PBE functional. There are clear similarities when compared with our results displayed in Figure 10. Firstly, both plots feature the VBM and CBM at the same positions. In addition, the bands' overall shape and curvature are strikingly similar, particularly in the regions of the Γ-M and Γ-K directions. In both plots, we observe a flat band near the Γ point, corresponding to a heavy effective mass. This flatness suggests a reduced dispersion in the bands and indicates out-of-plane electron transport in real space. Although the band gap in the PBE plot is smaller, this is consistent with the known tendency of the PBE functional to underestimate band gaps as discussed previously (3.2.6).

The similarity in the band shapes and effective masses between our plot and the one derived from the PBE functional further validates the accuracy of our results, as it demonstrates that our computational approach captures similar physical behaviour despite the slight difference in the predicted band gap. Therefore, the results from the computational method chosen for this investigation have been externally validated, and we can proceed to the strained calculations.

5.3 Band gap evolution under strain

In order to validate the stability and uniformity of the applied strain, the total energy of the ZrS_2 unit cell was calculated across a range of out-of-plane strains along the c-axis. Figure 12 shows the strain vs total energy curve, which displays a positive parabolic profile with the minimum energy occurring at 0% strain. This parabolic trend is both expected and physically meaningful, confirming that the unstrained structure corresponds to the system's equilibrium state. Both tensile and compressive strains result in a symmetrical increase in total energy. The strain vs. total energy plot for the in-plane a-b direction is provided in Appendix 23.
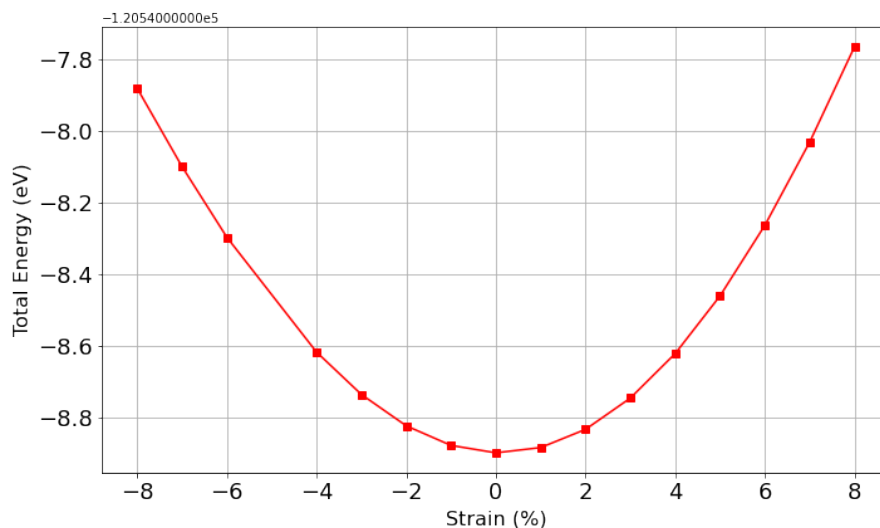

Figure 12: Total energy of ZrS_2 as a function of out-of-plane strain along the c-axis. The curve exhibits a positive parabolic shape with a minimum at 0% strain, indicating that the unstrained configuration corresponds to the system's equilibrium state and lowest energy.
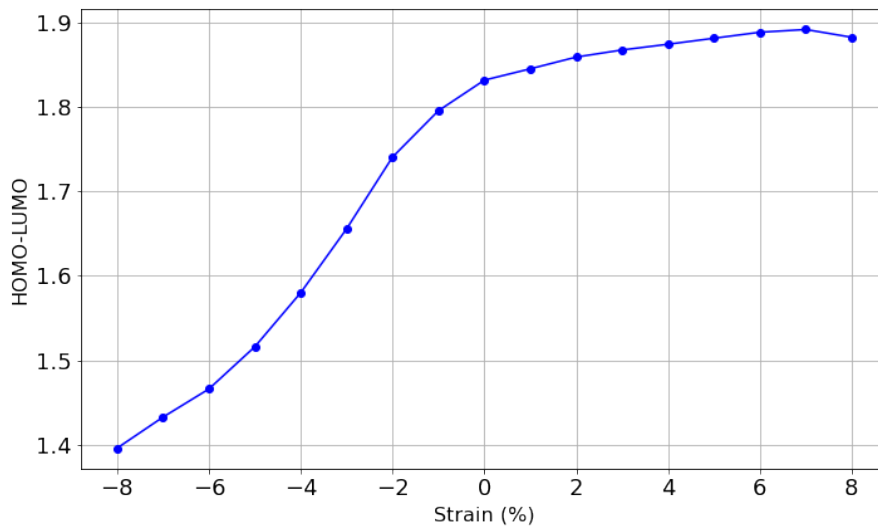
5.3.1 Biaxial In-Plane Strain

Figure 13: Dependence of the band gap of ZrS_2 on biaxial in-plane strain applied symmetrically along the a- and b-axes. The band gap decreases significantly under compressive strain and increases marginally under tensile strain.

Figure 13 presents the variation in the band gap of ZrS_2 as a function of biaxial strain applied symmetrically along the a- and b-axes. At 0% strain, a band gap of $1.83\,\text{eV}$ is observed, consistent with all previous calculations. Under compressive strain, the band gap increases gradually, reaching a maximum of $1.89\,\text{eV}$ at $+7\%$ strain. Beyond this point, the increase begins to reverse slightly. In contrast, tensile strain leads to a dramatic and non-linear decrease in the band gap, which drops to $1.40\,\text{eV}$ at -8% strain.
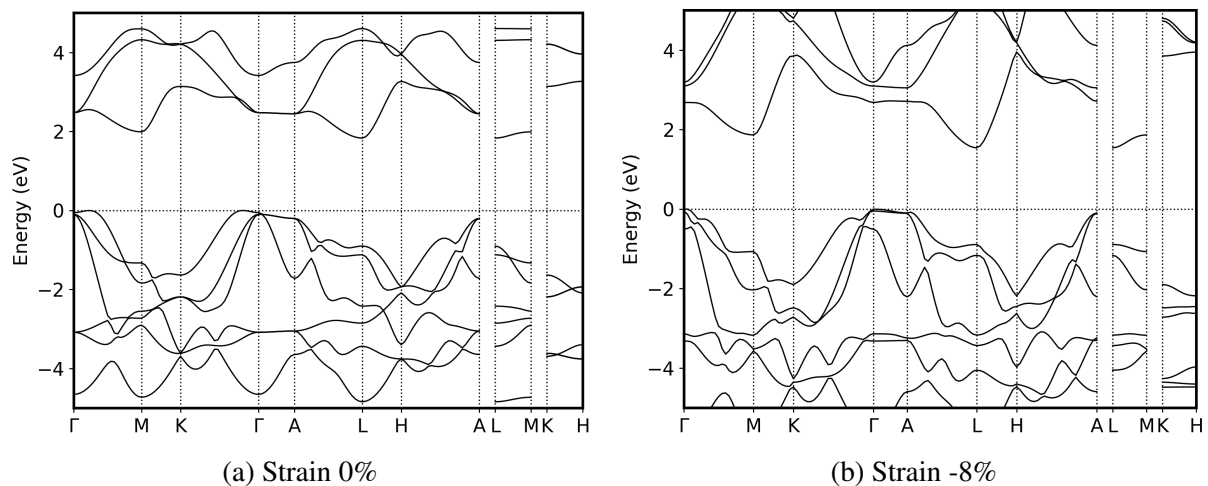

(a) Strain 0%

(b) Strain -8%

Figure 14: Band structure of ZrS_2 under biaxial strain applied symmetrically along the a- and b-axes. The band structure is displayed for both (a) zero applied strain and (b) tensile.

34

This asymmetric response can be understood by examining how strain influences atomic orbital interactions and hybridisation. Under compressive strain, the shortening of Zr–S bond lengths reduces in-plane lattice spacing and brings atomic orbitals closer together. However, due to repulsive interactions and orbital saturation, additional hybridisation is energetically unfavourable, resulting in only a modest increase in the band gap.

In contrast, tensile strain elongates the Zr–S bonds and distorts the trigonal prismatic coordination, altering the crystal field environment and enhancing orbital splitting. The weakened orbital overlap and increased lattice distortion lead to a more substantial band gap narrowing, as the VBM and CBM shift closer together. This behaviour is evident in the band structure diagrams shown in Figure 14, and is consistent with previous first-principles studies on strain-tunable band structures in ZrS_2 and related materials [68].

These trends align with strain-induced band modulation effects reported in other TMDs, such as MoS_2 and WS_2, where tensile strain reduces the band gap and can even drive an indirect-to-direct transition [69]. In Figure 14a, the VBM shifts from a position left of the Γ point to directly at Γ, indicating a qualitative change in band dispersion.

5.3.2 Uniaxial out-of-plane strain

The variation of the band gap of ZrS_2 as a function of out-of-plane strain applied along the crystallographic c-axis can be seen in Figure 15. The graph depicts an asymmetric response to compressive and tensile strain. The band gap increases under compression strain from $1.83\,\mathrm{eV}$ at 0% strain, peaking at $+5\%$ strain of $2.23\,\mathrm{eV}$, then beyond this, it exhibits a slight decline reaching $2.14\,\mathrm{eV}$ at $+8\%$ strain.
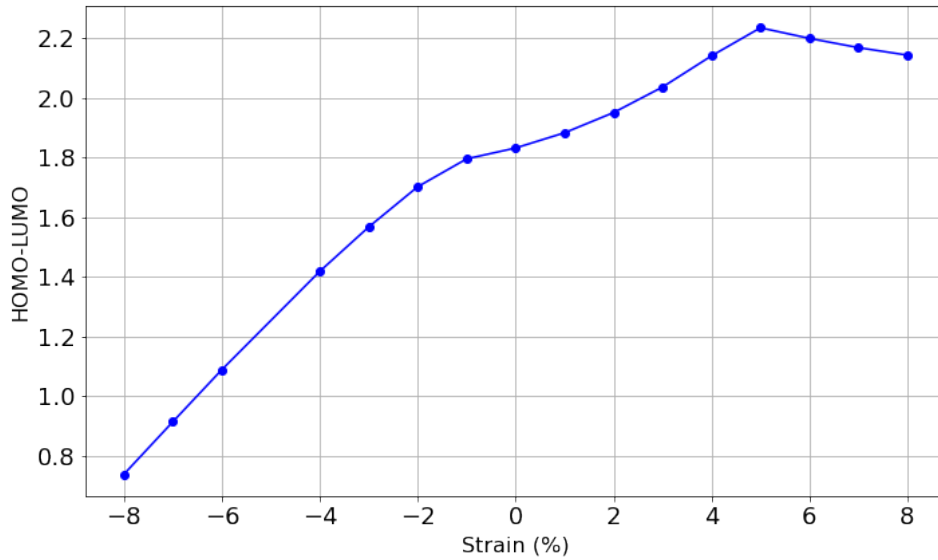
Figure 15: Dependence of the band gap of ZrS_2 on out-of-plane strain applied along the c-axis. The band gap increases with compressive strain up to approximately $+5\%$, beyond which it begins to slightly decrease. In contrast, the band gap exhibits a nearly linear decrease under tensile strain.

In contrast, the band gap decreases nearly linearly under tensile strain with increasing strain magnitude. This non-symmetric behaviour suggests distinct underlying physical mechanisms governing the electronic structure response under different strain conditions.

The increase in band gap under compressive strain could be attributed to reduced interlayer separation, which weakens orbital overlap between atomic layers. In particular, compression along the c-axis limits the interaction between sulphur p_z orbitals in neighbouring layers, thereby reducing band hybridisation at the valence and conduction band edges. This suppression of interlayer coupling leads to a widening of the band gap. A similar mechanism has been reported in a study on a ZrS_2/PtS_2 van der Waals heterostructure, where the authors observed a band gap increase under vertical compressive strain due to decreased interlayer interaction and reduced orbital mixing between layers [70].

Conversely, tensile strain expands the interlayer distance, enhancing interlayer interactions and facilitating greater hybridisation, narrowing the band gap. Such effects are well-documented in layered materials, particularly TMDs, where the electronic structure is susceptible to interlayer spacing and stacking order. We see a similar trend for the biaxial in-plane strain as previously mentioned [71].

It should be noted that the data point corresponding to -5% strain is missing. This omission is due to persistent non-convergence of the SCF calculation at that strain value. One plausible explanation is the emergence of electronic or structural instabilities at considerable tensile strain, potentially indicating proximity to a phase transition or mechanical instability. Additionally, the strain may induce near-degenerate states close to the Fermi level, complicating convergence due to competing orbital occupancies. Similar challenges have been reported in DFT studies, where strain-induced changes in electronic structure lead to convergence difficulties [72].

5.3.3 Semiconductor-to-metal transition

The uniaxial out-of-plane strain exhibited a clear linear decrease in the band gap between tensile strains of -4% and -8%, as illustrated in Figure 15. To quantitatively determine the onset of metallic behaviour, a line of best fit was applied to the calculated band gap values at -4%, -6%, -7%, and -8% tensile strains as shown in Figure 16.

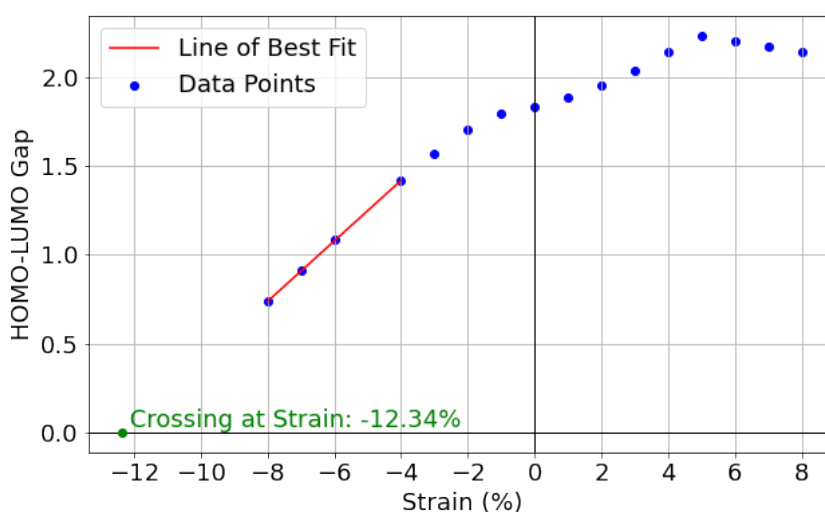Figure 16: Linear extrapolation of the band gap as a function of tensile c-axis strain in ZrS_2. The line of best fit predicts a semiconductor-to-metal transition at approximately -12.34% strain, where the band gap is expected to close.

The linear regression analysis yielded an extrapolated strain value of approximately -12.34%, at which the band gap is predicted to vanish, signalling the transition from a semiconductor to a metallic state. The observed linearity in the band gap trend within this strain range is consistent with previous predictions for strain-tunable TMDs [71].

To verify this extrapolated transition point, the atomic geometry corresponding to -12.34% strain was constructed and a DFT calculation was performed. The resulting band structure, Figure 17, indicated a minimal band gap of 0.02 eV, confirming that ZrS_2 is on the verge of metallic behaviour under this strain. The presence of a small, non-zero gap suggests a transition into a semi-metallic regime rather than a fully metallic state, a phenomenon also observed in other strained layered semiconductors [73].
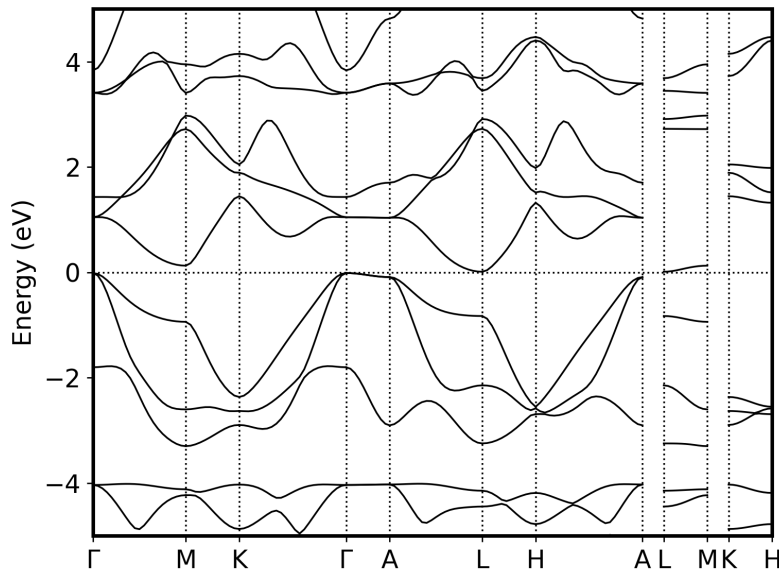
Figure 17: Electronic band structure of ZrS_2 at the predicted semiconductor-to-metal transition point under -12.34% tensile c-axis strain. The VBM is located at the Γ point, while the CBM occurs at the L point, indicating an indirect and nearly closed band gap.

These findings highlight the potential of c-axis strain as a tuning parameter for modulating the electronic phases of ZrS_2. The ability to drive a semiconductor-to-metal transition through mechanical deformation opens up new possibilities for strain-engineered electronic and optoelectronic devices. Such tunability is especially promising for applications in strain-gated transistors, sensors, and other flexible nanoelectronic systems [74].

5.4 Effective mass and carrier mobility under strain

The effective mass and carrier mobility of ZrS_2 were evaluated under varying strain along the in-plane biaxial and out-of-plane uniaxial directions. The calculations were performed for both holes and electrons, and the effective mass values were obtained from a Python package `Effmass` [32] that utilises the least squares fit method on the band structure plot curves to determine the curvature in effective mass. The mobility was calculated using the obtained effective masses using the deformation potential theory.

5.4.1 Biaxial in-plane strain

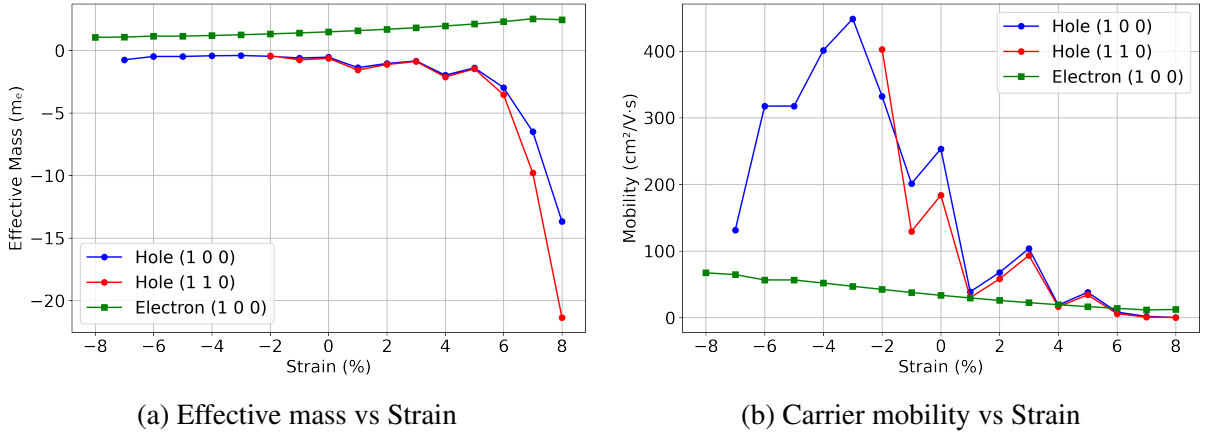(a) Effective mass vs Strain   (b) Carrier mobility vs Strain

Figure 18: (a) Effective mass of electrons and holes along the ab-axis as a function of in-plane strain. (b) Corresponding carrier mobility calculated using the deformation potential theory.

The plot of the effective mass and carrier mobility as a function of strain, shown in Figure 18, demonstrates a clear dependence on the applied strain. For holes, the effective mass generally increases with tensile strain, leading to a reduction in mobility. At 0% strain, the effective mass in the [1 0 0] direction is -0.54 m_e, with a corresponding mobility of 253.29 cm^2/Vs. However, at +8% strain, the effective mass increases significantly to -13.67 m_e, resulting in a drastic decrease in mobility to just 0.40 cm^2/Vs. Similarly, in the [1 1 0] direction, the effective mass rises from -0.63 m_e at 0% strain to -21.35 m_e at +8% strain, with the mobility dropping from 183.74 cm^2/Vs to just 0.16 cm^2/Vs.

For compressive strain, the opposite trend is observed. The hole effective mass decreases, resulting in increased mobility. At -4% strain, the effective mass is -0.43 m_e, and the mobility reaches a high value of 401.36 cm^2/Vs. At -3% strain, the hole effective mass is even lower at -0.41 m_e, with mobility peaking at 448.58 cm^2/Vs. This suggests that compressive strain can significantly enhance hole mobility.

For electrons, the effective mass and mobility also show strain dependence but to a lesser extent than holes. At 0% strain, the electron effective mass in the [1 0 0] direction is 1.48 m_e, with a mobility of 33.50 cm^2/Vs. As the tensile strain increases to +8%, the effective mass rises to 2.46 m_e, with the mobility decreasing to 12.24 cm^2/Vs. Under compressive strain, the electron effective mass decreases, reaching 1.05 m_e at -8% strain, with an associated mobility of 67.25 cm^2/Vs.
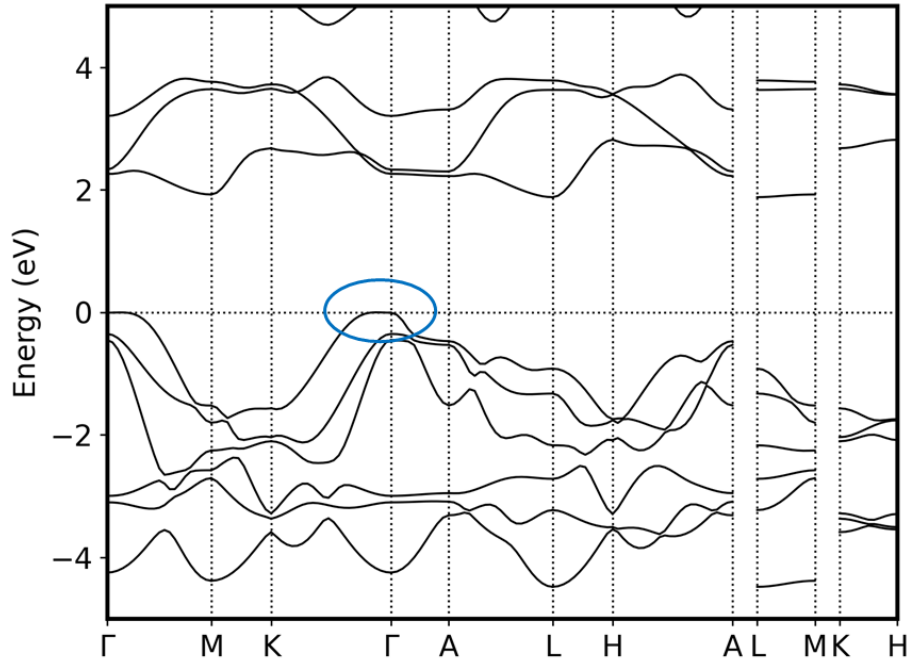
Figure 19: Band structure of ZrS$_2$ at $+5\%$ biaxial in-plane strain, highlighting the effect on carrier dispersion.

The band structure at +5% strain, Figure 19, shows that the valence band becomes flatter compared to the conduction band, indicating an increase in the hole effective mass. The electron bands maintain more curvature, which corresponds to lower effective mass and higher mobility.

Overall, the results indicate that tensile strain tends to reduce carrier mobility by increasing the effective masses, especially for holes. In contrast, compressive strain decreases the effective masses and thereby enhances mobility.

5.4.2 Uniaxial out-of-plane strain

(a) Effective mass vs Strain

(b) Carrier mobility vs Strain

Figure 20: (a) Effective mass of electrons and holes along the c-axis as a function of out-of-plane strain. (b) Corresponding carrier mobility calculated using the deformation potential theory.

The effective mass of holes remains nearly constant across the entire strain range, with values consistently around $-4.15\,m_e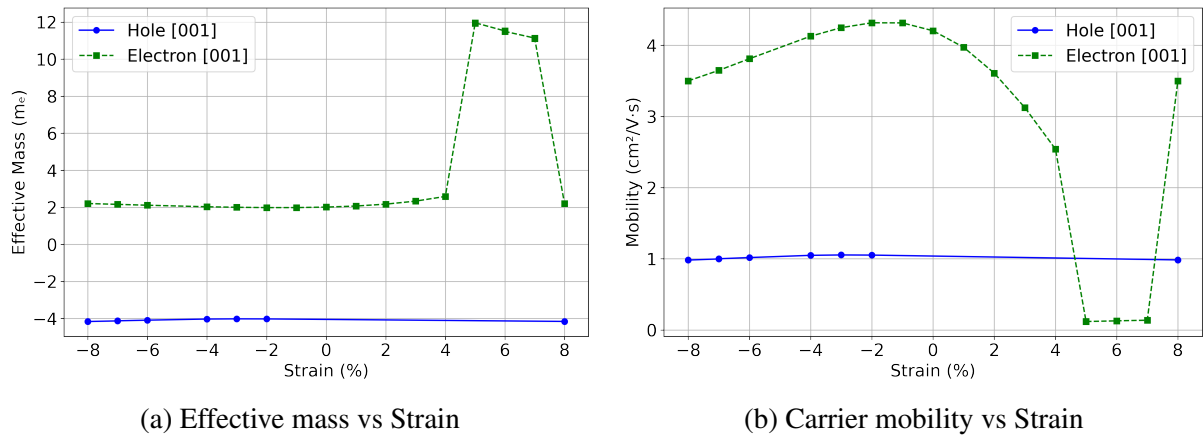$, as shown on the left side of Figure 20. For instance, at -8% strain, the hole effective mass is approximately $-4.16\,m_e$, while at $+8\%$ strain, it remains essentially unchanged at $-4.16\,m_e$. This consistency suggests that the VBM curvature is largely preserved under compressive and tensile strain, indicating a high degree of structural and electronic stability. Consequently, hole transport is expected to be relatively unaffected by out-of-plane strain, reflecting minimal sensitivity to mechanical deformation along the c-axis.

Notably, no effective mass values were extracted for holes in the [0 0 1] direction between -1% and $+7\%$ strain. This absence may be attributed to a strain-induced shift in the VBM in reciprocal space, which can move away from the high-symmetry path used for mass extraction and render the effective mass along [0 0 1] physically meaningless under those conditions. Additionally, band degeneracy or hybridisation with nearby valence bands under moderate strain may induce significant deviations from parabolic behaviour, leading to poor fits or numerical instabilities during post-processing with tools such as `effmass`. In some instances, the band dispersion becomes nearly flat, and the corresponding energy variations between sampled k-points fall below numerical precision, making the second derivative, and hence the effective mass, ill-defined.

In contrast, the effective mass of electrons is significantly more sensitive to strain. At -8% strain, the electron effective mass is approximately $2.21\,m_e$, steadily decreasing to $2.00\,m_e$ at -3% strain. This trend indicates that compressive strain initially reduces the electron effective mass, enhancing mobility. However, the effective mass sharply increases with further compression, reaching a peak value of $11.94\,m_e$ at $+5\%$ strain. This non-monotonic behaviour suggests substantial changes to the CBM as the lattice is distorted, likely involving strain-induced shifts in band edge curvature or band reordering phenomena. Beyond $+5\%$ strain, the effective mass decreases again as strain increases to $+8\%$, which returns to approximately $2.21\,m_e$.

(a) Band structure at $+4\%$ uniaxial out-of-plane strain.

(b) Band structure at $+6\%$ uniaxial out-of-plane strain.
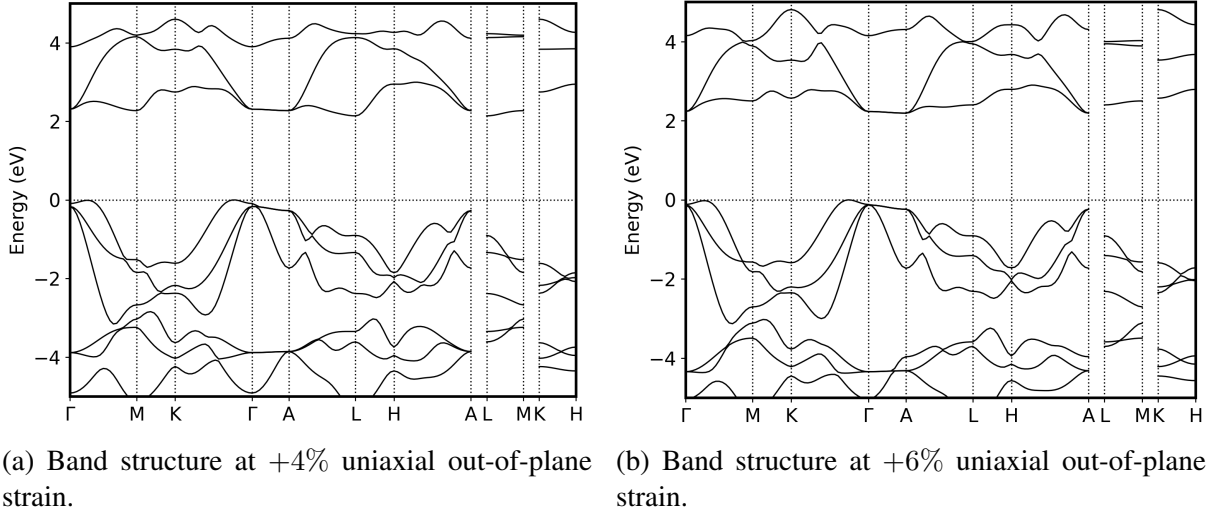
Figure 21: Comparison of the band structure of ZrS_2 under different uniaxial out-of-plane strains. (a) The band structure at $+4\%$ strain shows a certain positioning of the CBM, while (b) at $+6\%$ strain, a significant shift in the CBM from lattice vector **L** to **A** is observed. This shift correlates with the non-monotonic behaviour of the electron effective mass.

This behaviour can be attributed to a shift in the CBM, as observed in the band structure plots comparing the $+4\%$ and $+6\%$ strain cases (see **??**). The transition corresponds to a notable change in the position of the CBM along the Brillouin zone, specifically from the lattice vector $\mathbf{L}$ to $\mathbf{A}$. Such a shift indicates that the electronic states near the CBM become increasingly localised along different crystal directions as strain is varied, resulting in significant modifications to the curvature of the conduction band.

The mobility trends for holes and electrons reflect the observed changes in effective mass. For holes, the carrier mobility remains almost constant throughout the strain range, with values around $1.0\,\mathrm{cm}^2/\mathrm{Vs}$. This stability mirrors the flat trend observed in the hole effective mass and confirms that hole transport is unaffected mainly by strain along the c-axis.

Conversely, electron mobility exhibits a pronounced dependence on strain. Starting from $3.50\,\mathrm{cm}^2/\mathrm{Vs}$ at -8% strain, the mobility increases to a maximum of approximately $4.32\,\mathrm{cm}^2/\mathrm{Vs}$ at -2% strain, reflecting the initial decrease in effective mass. However, as the strain becomes more compressive and the effective mass increases, the mobility drops dramatically to just $0.12\,\mathrm{cm}^2/\mathrm{Vs}$ at $+5\%$ strain. This decrease is consistent with the substantial increase in effective mass at this strain level. Subsequently, the electron mobility slightly recovers as the strain reaches $+8\%$, rising to approximately $3.50\,\mathrm{cm}^2/\mathrm{Vs}$.

Overall, the results demonstrate that while hole mobility in ZrS_2 remains robust under out-of-plane strain, electron mobility is significantly modulated, particularly under intense compressive deformation. The sharp increase in electron effective mass around $+5\%$ strain indicates a possible electronic transition or band reordering, highlighting the critical influence of lattice distortions on carrier transport properties along the c-axis.

5.5 Discussion

5.5.1 Strain-dependent band gap behaviour

The band gap of a semiconductor is a key determinant in its efficiency as a photovoltaic (PV) material. The Shockley–Queisser limit provides a theoretical upper bound on the efficiency of a single-junction solar cell, which is primarily determined by the material's band gap. For single-junction PV cells under standard solar illumination, the optimal band gap for maximum theoretical efficiency is approximately $1.34\,\mathrm{eV}$ [75]. A material with a band gap close to this value absorbs a broad portion of the solar spectrum, while also minimising thermalisation losses, which occur when high-energy photons generate electrons that quickly lose excess energy.
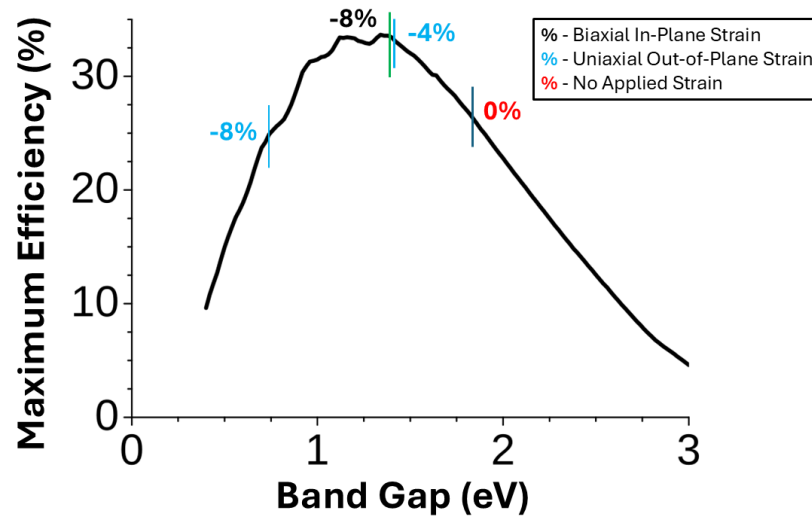

Figure 22: Shockley-Queisser limit of efficiency for a single-junction solar cell as a function of the band gap energy. The graph shows the theoretical maximum efficiency that can be achieved for a given band gap, with the peak efficiency occurring around $1.34\,\mathrm{eV}$. Band gap points corresponding to ZrS_2 at different strains are included: -8% and -4% out-of-plane strain, 0% strain for unstrained ZrS_2, and -8% in-plane strain. Adapted from [75].

As previously discussed (5.2), at 0% strain, ZrS_2 possesses a band gap of $1.83\,\mathrm{eV}$, which is above the ideal value for single-junction PV devices, as shown in Figure 22. This gap leads to suboptimal absorption of solar energy, as a significant portion of the solar spectrum lies below the material's absorption threshold. However, the ability to modulate the band gap through strain opens new opportunities for tailoring ZrS_2 for use in PV applications.

Under tensile biaxial strain, the band gap of ZrS_2 decreases significantly. At -8% strain, the band gap drops to $1.40\,\mathrm{eV}$, which brings the material much closer to the optimal range for single-junction solar cells. This reduction in band gap is primarily due to the elongation of the Zr–S bonds, which distorts the crystal field and weakens orbital overlap between the valence and conduction bands. As a result, the CBM and VBM move closer together, narrowing the band gap. This strain-induced reduction in band gap can improve the absorption of lower-energy photons, increasing the photocurrent and overall PV performance.

In contrast, the band gap increases gradually under compressive biaxial strain, reaching a maximum of $1.89\,\mathrm{eV}$ at $+7\%$ strain. While this increase in band gap moves ZrS_2 further from

the optimal PV range, it could still be beneficial in specific applications, such as in multi-junction tandem solar cells, where materials with larger band gaps are used in the top cell to capture higher-energy photons. This trend, in which the band gap increases with compression, is linked to the shortening of the Zr–S bond lengths and the reduced hybridisation between atomic orbitals, leading to a widening band gap.

The out-of-plane tensile strain applied along the c-axis also has a pronounced effect on the electronic properties of ZrS$_2$. Under tensile strain along this direction, the band gap decreases nearly linearly, similar to the behaviour observed under biaxial tensile strain. At -8% tensile strain along the c-axis, the band gap reaches $1.40\,\text{eV}$, further reinforcing the trend of band gap reduction under tensile strain. This decrease in band gap is likely due to an increased distortion of the trigonal prismatic coordination of the ZrS$_2$ structure, which weakens the orbital overlap between neighbouring sulphur atoms. The expanded interlayer distance in the c-axis direction promotes greater hybridisation of orbitals, narrowing the electronic band gap.

The band gap variation under both biaxial and uniaxial strain suggests that ZrS$_2$ could be engineered to optimise its band gap for various photovoltaic applications. For single-junction PV cells, tensile strain could bring the material's band gap closer to the optimal value, improving solar cell efficiency. However, for multi-junction devices, compressive strain may be more appropriate due to the wider band gap, which could be used as the top cell in tandem architectures, where materials with larger band gaps are crucial for absorbing higher-energy photons and improving overall efficiency.

5.5.2 Effective mass and carrier transport

Carrier mobility is governed by both the effective mass and scattering mechanisms. While scattering was not explicitly modelled, curvature effective masses were computed to assess the intrinsic transport tendencies under strain. Electron effective masses ranged from approximately $2\,m_e$ (unstrained) to over $10\,m_e$ under high tensile strain, while hole effective masses, initially very large (over $4\,m_e$), showed some reduction under tension.

These trends indicate a trade-off: while tensile strain increases the band gap, it severely reduces electron mobility due to band flattening near the CBM. Compressive strain improves electron mobility but at the expense of narrowing the band gap. This dual effect highlights a key result: optimal strain must balance transport and optical properties, not maximise either in isolation.

A novel insight from these results is the identification of a strain "sweet spot" around -2% to -4% tensile c-axis strain, where the band gap is enhanced and hole effective mass reduced without excessively degrading electron transport. This regime offers a practical design target for device engineers seeking to optimise p-type performance or reduce the n/p mobility asymmetry.

5.5.3 Comparison to literature and relevance of strain direction

Most prior work on TMD strain engineering has focused on biaxial or in-plane uniaxial strain, due to its stronger coupling to the intralayer bonding network [76, 77]. In contrast, we focused on out-of-plane strain, which is experimentally accessible via substrate bending, pressure application, or heterostructure stacking. Although the effect on the electronic structure is less dramatic than in-plane strain, the results confirm that c-axis strain provides a tunable and reversible handle for modulating band alignment and effective mass without fundamentally altering crystal symmetry or bonding.

In future studies, extending this analysis to biaxial or in-plane uniaxial strain is likely to reveal more pronounced shifts in the band structure, including possible indirect-to-direct transitions, as reported in monolayer MoS_2 [78] and others. Combining out-of-plane and in-plane strain could enable multidimensional optimisation of band gap, effective mass, and optical absorption, a novel approach largely unexplored in the context of ZrS_2 or TMDs more generally.

5.5.4 Future directions

While the present results provide valuable insight into the strain-dependent electronic behaviour of bulk ZrS_2, there are key limitations in the methodology that should inform interpretation and motivate future work. Notably, the calculations presented here do not include an explicit treatment of van der Waals (vdW) interactions. This is a significant omission in layered materials such as ZrS_2, where interlayer bonding is governed primarily by weak dispersion forces. Neglecting vdW corrections likely overestimates the equilibrium interlayer spacing and may affect the accuracy of trends observed under c-axis strain, especially in the tensile regime where layers are further separated.

Future studies should therefore implement vdW-inclusive methods, such as the DFT-D3 correction [79], the Tkatchenko–Scheffler scheme [80], or non-local vdW functionals like optB88-vdW [81]. Incorporating these would yield more realistic interlayer distances and may shift the strain thresholds at which notable changes in the electronic structure occur. Given the relatively weak coupling between layers in ZrS_2, it is expected that vdW corrections would not qualitatively alter the trends but would refine the quantitative predictions, especially in identifying the strain ranges of maximal band gap tuning or optimal effective mass.

Another area for further development is the analysis of charge densities and orbital character. While this work focused on band edge energies and curvature effective masses, it did not directly examine the spatial distribution of charge carriers or the nature of the bonding under strain. A detailed investigation into charge density differences between strained and unstrained structures could illuminate how orbital hybridisation and interlayer charge redistribution evolve, particularly at the valence and conduction band edges. This would enhance understanding of the microscopic mechanisms underpinning the observed changes in effective mass and band structure, and could reveal opportunities for interfacial engineering or defect-tolerant design.

Moreover, isosurface plots of charge density and partial density of states (PDOS) could clarify whether particular orbitals (e.g., Zr d or S p states) are more strain-sensitive, and how these contribute to band edge modulation. Combined with projected band structure analysis, this would help establish whether strain induces any indirect-to-direct transitions in monolayer or bilayer forms, an avenue worth pursuing given the known strain tunability in related TMDs.

In summary, while the current work establishes a clear and reproducible framework for exploring strain effects in ZrS$_2$, incorporating vdW corrections and charge density analysis would significantly deepen the physical insight and strengthen the connection between structural perturbation and electronic behaviour.

5.5.5 Scientific and technological significance

The synthesis of results across band gap, effective mass, and strain regimes leads to a central conclusion: strain engineering in ZrS$_2$ is a viable tool for tuning electronic properties, but optimal regimes lie in moderate rather than extreme strain ranges. This insight is critical for practical device design, where extreme strain is often challenging to apply uniformly or reversibly.

From a technological perspective, ZrS$_2$ under mild tensile c-axis strain shows promise as a tunable absorber layer in photovoltaic devices, or as part of strain-sensitive electronic or sensor components. Its stable indirect band gap and strain-resilient structure make it an attractive candidate for flexible electronics and low-cost, strain-engineered optoelectronics.

6   Conclusion

This work has explored the electronic properties of ZrS_2 under strain, focusing on the strain effects along the c-axis. Through density functional theory (DFT) calculations, the band gaps and carrier transport properties of ZrS_2 were analysed, offering insights into their potential application in photovoltaic devices. The results presented in this report contribute to a deeper understanding of the material's behaviour under mechanical stress, providing important implications for strain engineering in two-dimensional materials for next-generation energy applications.

The primary aim of this report was to investigate how strain affects the electronic structure of ZrS_2 and to explore the implications for its use in photovoltaic devices. The objectives outlined in the introduction were successfully achieved by applying the PBE and HSE06 functionals, performing effective mass analysis, and calculating the carrier mobility under various strain conditions. The results indicate that strain engineering can significantly influence the material's carrier mobility and band gap, making ZrS_2 a promising candidate for photovoltaic applications, remarkably when fine-tuned under strain.

One of the key findings from this work was the variation in effective mass with strain. The electron effective masses were found to increase under tensile strain, which could lead to decreased mobility, while hole effective masses exhibited a more significant dependence on strain. The variation of the band gap with strain was also observed, with tensile strain leading to a narrowing of the band gap, which aligns with previous studies in the literature. These findings corroborate the hypothesis that strain can be an effective tool for modifying the electronic properties of materials for photovoltaic applications but also highlight the complex relationship between strain and material behaviour.

When comparing the results obtained in this study with the literature, it is evident that while the behaviour of ZrS_2 under strain has been explored in previous works, this study provides a more detailed and systematic approach using the PBE and HSE06 functionals. The observed trends in effective mass and band gap evolution align with studies on similar TMDs, but the detailed analysis of the strain dependence on carrier transport properties, particularly the mobility calculations, has not been extensively explored for ZrS_2. This work fills that gap in the literature, offering a more complete understanding of ZrS_2's potential in photovoltaic devices.

The success of this project is evident in the clear achievement of the research objectives outlined in the introduction. Using DFT to model the strain effects on ZrS_2 provided valuable insights into how this material can be optimised for photovoltaic applications. Furthermore, the study's comprehensive analysis of carrier mobility and the band gap under various strain conditions contributes novel data to the field of material science. However, while the results are promising, there are limitations to this study that should be addressed in future work.

One notable limitation is the absence of experimental validation. The findings of this study are based solely on computational methods. While DFT calculations are powerful, they are not immune to errors associated with approximations in the exchange-correlation functionals and the chosen computational parameters. Future work could focus on experimental studies of ZrS_2 under strain, particularly using angle-resolved photoemission spectroscopy (ARPES) to observe the strain-induced changes in the electronic structure directly. Additionally, more advanced computational methods, including many-body effects or hybrid functionals, could be employed to refine the results and account for the limitations of the current models.

Another avenue for future research lies in exploring the effects of strain on the optoelectronic

properties of ZrS_2. While this study focused on the electronic structure and carrier transport properties, the optical properties, such as absorption spectra and exciton dynamics, also play a crucial role in photovoltaic performance. Strain could modulate the absorption properties of ZrS_2, and investigating this in more detail could lead to further optimisation for photovoltaic applications. Moreover, incorporating the effects of environmental factors such as temperature and humidity could provide a more comprehensive picture of how ZrS_2 behaves under real-world conditions.

In conclusion, this dissertation has successfully investigated the electronic properties of ZrS_2 under strain, providing valuable insights into the material's potential for use in photovoltaic devices. The results demonstrate that strain engineering can significantly alter the electronic structure and carrier transport properties of ZrS_2, which could be leveraged to enhance its performance in energy applications. However, the study also highlights the need for further research, particularly experimental validation and exploration of the material's optoelectronic properties, to realise the potential of ZrS_2 in practical applications fully. This work lays the foundation for future studies that could lead to the development of novel materials for sustainable energy solutions.

7 References

References

[1] IPCC. Climate change 2023: Synthesis report. *Intergovernmental Panel on Climate Change*, 2023.

[2] Johan Rockström et al. A safe operating space for humanity. *Nature*, 461(7263):472–475, 2009.

[3] Olivier Vidal, Bruno Goffé, and Nicholas Arndt. Metals for a low-carbon society. *Nature Geoscience*, 6(11):894–896, 2013.

[4] Thomas E. Graedel et al. Criticality of metals and metalloids. *Proceedings of the National Academy of Sciences*, 112(14):4257–4262, 2015.

[5] Beate Achzet and Christoph Helbig. Supply risks associated with rare earth elements and emerging technologies. *Resources Policy*, 38(4):472–481, 2013.

[6] Marijn LCM Henckens, Ernst Worrell, and Kornelis Blok. Global resource use: Towards a more sustainable and equitable future. *Resources, Conservation and Recycling*, 107:92–97, 2016.

[7] International Energy Agency. The role of critical minerals in clean energy transitions, 2021. Accessed: 2025-05-07.

[8] Anubhav Jain, Shyue Ping Ong, Geoffroy Hautier, et al. Commentary: The materials project: A materials genome approach to accelerating materials innovation. *APL Materials*, 1(1):011002, 2013.

[9] Stefano Curtarolo, Wahyu Setyawan, Sohrab Wang, et al. The high-throughput highway to computational materials design. *Nature Materials*, 12(3):191–201, 2013.

[10] Thomas Heine. Transition metal chalcogenides: Ultrathin inorganic materials with tunable electronic properties. *Accounts of Chemical Research*, 48(1):65–72, 2015.

[11] Rafael Roldán, Andres Castellanos-Gomez, Emmanuele Cappelluti, and Francisco Guinea. Strain engineering in semiconducting two-dimensional crystals. *Journal of Physics: Condensed Matter*, 27(31):313201, 2015.

[12] Manish Chhowalla, Hyeon Suk Shin, Goki Eda, et al. The chemistry of two-dimensional layered transition metal dichalcogenide nanosheets. *Nature Chemistry*, 5(4):263–275, 2013.

[13] Sajedeh Manzeli, Dmitry Ovchinnikov, Didier Pasquier, Oleg V Yazyev, and Andras Kis. 2d transition metal dichalcogenides. *Nature Reviews Materials*, 2(8):17033, 2017.

[14] J. A. Wilson and A. D. Yoffe. The transition metal dichalcogenides discussion and interpretation of the observed optical, electrical, and structural properties. *Advances in Physics*, 18(73):193–335, 1969.

[15] Appalakondaiah Gandi and Udo Schwingenschlögl. Thermoelectric properties of bulk and monolayer mos and ws. *Journal of Materials Chemistry C*, 4(15):3555–3560, 2016.

[16] WJ Schutte and JL De Boer. Crystal structures of tungsten disulfide and diselenide and related compounds. *Journal of Solid State Chemistry*, 70(2):207–209, 1987.

[17] Jun Kang, Sefaattin Tongay, Jianmin Li, and Junqiao Wu. Electronic structure and optical properties of monolayer transition metal dichalcogenides mx (m= ti, zr, hf; x= s, se, te). *Journal of Applied Physics*, 117(11):114302, 2015.

[18] Wei Zhang, Ying Yu, Bei Chen, and Shuang Li. Electronic structures and optical properties of strained monolayer group ivb transition metal dichalcogenides. *Scientific Reports*, 7:4966, 2017.

[19] Anil Kumar and P. K. Ahluwalia. Electronic structure of transition metal dichalcogenides monolayers 1h-mx (m= mo, w; x= s, se, te). *European Physical Journal B*, 87(8):1–7, 2014.

[20] Priya Johari and Vijay B. Shenoy. Tuning the electronic properties of semiconducting transition metal dichalcogenides by applying mechanical strains. *ACS Nano*, 6(6):5449–5456, 2012.

[21] Emilio Scalise, Mohamed Houssa, Geoffrey Pourtois, Valery V Afanas'ev, and Andre Stesmans. Strain-induced semiconductor to metal transition in the two-dimensional honeycomb structure of mos. *Nano Research*, 5(1):43–48, 2012.

[22] Ashwin Ramasubramaniam, Daniel Naveh, and Elias Towe. Tunable band gaps in bilayer graphene by strain. *Physical Review B*, 84(20):205325, 2011.

[23] Mahdi Ghorbani-Asl, Nourdine Zibouche, Mohammad Wahiduzzaman, Ana F Oliveira, Agnieszka Kuc, and Thomas Heine. Strain engineering of the electronic and optical properties of monolayer and bilayer mos. *Physical Review B*, 88(24):245440, 2013.

[24] Hartwin Peelaers and Chris G Van de Walle. Effects of strain on band structure and effective masses in mos. *Physical Review B*, 86(24):241401, 2012.

[25] Hiram J. Conley, Bin Wang, Jed I. Ziegler, et al. Bandgap engineering of strained monolayer and bilayer mos. *Nano Letters*, 13(8):3626–3630, 2013.

[26] W. S. Yun, S. W. Han, S. C. Hong, I. G. Kim, and J. D. Lee. Thickness and strain effects on electronic structures of transition metal dichalcogenides: 2h-mx semiconductors (m= mo, w; x= s, se, te). *Physical Review B*, 85(3):033305, 2012.

[27] Minglei Kan, Jianli Wang, Xian-Bin Li, Shunhong Zhang, Yafei Li, Yoshiyuki Kawazoe, Purusottam Jena, and Qiang Sun. Structures and phase transition of a mos monolayer under tensile and compressive strain. *Journal of Physical Chemistry C*, 118(3):1515–1522, 2014.

[28] Junfeng He, Kerstin Hummer, and Cesare Franchini. Strain-induced isostructural phase transition in monolayer mos. *Physical Review B*, 89(7):075409, 2014.

[29] Vitor M. Pereira and A. H. Castro Neto. Strain engineering of graphene's electronic structure. *Physical Review Letters*, 103(4):046801, 2009.

[30] Simon M. Sze and Ming-Kwei Lee. *Semiconductor Devices: Physics and Technology*. Wiley, 3rd edition, 2012.

[31] L. M. Zhang, W. B. Zhang, S. Qiao, Y. Yang, J. M. Shang, and S. Q. Feng. Two-dimensional zrse2/zrs2 heterobilayer tuned by electric field for optoelectronic devices. *Journal of the Korean Physical Society*, 80(7):606–612, 2022.

[32] Lucy D. Whalley, Jarvist M. Frost, Benjamin J. Morgan, and Aron Walsh. Impact of non-parabolic electronic band structure on the optical and transport properties of photovoltaic materials. *arXiv preprint arXiv:1811.02281*, 2019. Dated: February 1, 2019.

[33] Feliciano Giustino. *Materials Modelling using Density Functional Theory*. Oxford University Press, 2014.

[34] David J. Griffiths. *Introduction to Quantum Mechanics*. Pearson, 3rd edition, 2016.

[35] N. M. Harrison. An introduction to density functional theory, 1999. Accessed: 2024-11-18.

[36] Douglas R. Hartree. The wave mechanics of an atom with a non-coulomb central field. part i. theory and methods. *Mathematical Proceedings of the Cambridge Philosophical Society*, 24(1):89–110, 1928.

[37] Pierre Hohenberg and Walter Kohn. Inhomogeneous electron gas. *Physical Review*, 136(3B):B864–B871, 1964.

[38] Volker Blum, Ralf Gehrke, Felix Hanke, Paula Havu, Ville Havu, Xinguo Ren, Karsten Reuter, and Matthias Scheffler. Ab initio molecular simulations with numeric atom-centered orbitals. *Computer Physics Communications*, 180(11):2175–2196, 2009.

[39] Walter Kohn and Lu Jeu Sham. Self-consistent equations including exchange and correlation effects. *Physical Review*, 140(4A):A1133, 1965.

[40] Paolo Giannozzi. Quantum espresso: An overview and recent developments. `http://qe2019.ijs.si/talks/Giannozzi_Day1.pdf`, 2019.

[41] Rajendra P. Joshi, Andrew D. McNaughton, Dennis G. Thomas, Christopher S. Henry, Samuel Canon, Lee Ann McCue, and Neeraj Kumar. Quantum mechanical methods predict accurate thermodynamics of biochemical reactions. *ACS Omega*, 6(14):9948–9959, 2021. Accessed: 2025-05-07.

[42] Axel D Becke. A new mixing of hartree–fock and local density-functional theories. *The Journal of Chemical Physics*, 98(2):1372–1377, 1993.

[43] John P. Perdew, Kieron Burke, and Matthias Ernzerhof. Generalized gradient approximation made simple. *Phys. Rev. Lett.*, 77:3865–3868, Oct 1996.

[44] John P. Perdew, Kieron Burke, and Matthias Ernzerhof. Generalized gradient approximation made simple. *Physical Review Letters*, 77(18):3865–3868, 1996.

[45] J. Heyd, G. E. Scuseria, and M. Ernzerhof. Hybrid functionals based on a screened coulomb potential. *The Journal of Chemical Physics*, 118(18):8207–8215, 2003.

[46] A.D. Becke. Density-functional exchange-energy approximation with correct asymptotic behavior. *Physical Review A*, 38(6):3098–3100, 1988.

[47] John P. Perdew and Yue Wang. Accurate and simple analytic representation of the electron-gas correlation energy. *Physical Review B*, 33(12):8800–8802, 1986.

[48] Jianwei Cui, Xin Liu, Yanjing Wang, Daming Zhang, and Xiaolong Li. First principles study of the electronic structure and optical properties of monolayer and bilayer phosphorene. *Nature Communications*, 10(1):1–9, 2019.

[49] Jochen Heyd, Gustavo E Scuseria, and Matthias Ernzerhof. Hybrid exchange-correlation functional for condensed systems. *The Journal of Chemical Physics*, 118(18):8207–8215, 2003.

[50] Wahyu Setyawan and Stefano Curtarolo. High-throughput electronic band structure calculations: Challenges and tools. *Computational Materials Science*, 49(2):299–312, August 2010.

[51] Jake Procter. Zrs$_2$-strain: Tailoring electronic properties via strain engineering, 2025. Dataset on Zenodo.

[52] Anubhav Jain, Shyue Ping Ong, Geoffroy Hautier, Wei Chen, and et al. Commentary: The materials project: A materials genome approach to accelerating materials innovation. *APL Materials*, 1(1):011002, 2013.

[53] Ask Hjorth Larsen, Jens Jørgen Mortensen, Jakob Blomqvist, and et al. The atomic simulation environment—a python library for working with atoms. *Journal of Physics: Condensed Matter*, 29(27):273002, jun 2017.

[54] H. Y. Lv, W. J. Lu, D. F. Shao, H. Y. Lu, and Y. P. Sun. Strain-induced enhancement in the thermoelectric performance of a zrs2 monolayer. *J. Mater. Chem. C*, 4:4538–4545, 2016.

[55] Lucy D. Whalley. effmass: An effective mass package. *Journal of Open Source Software*, 3(28):797, 2018.

[56] John Bardeen and William Shockley. Deformation potentials and mobilities in non-polar crystals. *Physical Review*, 80(1):72–80, 1950.

[57] Q. Zhao et al. Elastic, electronic, and dielectric properties of bulk and monolayer zrs, zrse, hfs, hfse from van der waals density-functional theory. *Physica Status Solidi B*, 254(5):1700033, 2017.

[58] Kristen Kaasbjerg, Kristian S Thygesen, and Antti-Pekka Jauho. Acoustic phonon limited mobility in two-dimensional semiconductors: Deformation potential and piezoelectric scattering in monolayer mos$_2$ from first principles. *Physical Review B*, 85(11):115317, 2012.

[59] Yan Peng, Hao Zeng, Huan Zhao, Weng Huang, Hengyu Li, Jia Zeng, Yanling Ma, Zheng Liang, and Xiang Yan. Strain-engineering of the electronic properties of two-dimensional materials. *Scientific Reports*, 4, 2014.

[60] John Bardeen and William Shockley. Deformation potentials and mobilities in non-polar crystals. *Physical Review*, 80(1):72–80, 1950.

[61] John D. Hunter. Matplotlib: A 2d graphics environment. *Computing in Science & Engineering*, 9(3):90–95, 2007.

[62] Yan Li, Jun Kang, and Jingbo Li. Indirect-to-direct band gap transition of the zrs2 mono-layer by strain: first-principles calculations. *RSC Adv.*, 4:7396–7401, 2014.

[63] Xin Luo, Michael B. Sullivan, and Su Ying Quek. First principles investigations of the atomic, electronic, and thermoelectric properties of equilibrium and strained bi_2se_3 & bi_2te_3, with van der waals interactions. *arXiv:1308.1523*, 2013.

[64] Kenneth S. Burch, David Mandrus, and Je-Geun Park. Magnetism in two-dimensional van der waals materials. *Nature*, 563:47–52, 2018.

[65] Mohamed Moustafa, Alexander Paulheim, Christoph Janowitz, and Recardo Manzke. Band structure of zrsse by arpes, Jul 2011.

[66] Edoardo Martino, David Santos-Cottin, Florian Le Mardelé, and et al. Structural phase transition and bandgap control through mechanical deformation in layered semiconduc-tors 1t–zrx (x = s, se). *ACS Materials Letters*, 2(9):1115–1120, 2020.

[67] K. F. Mak, C. Lee, J. Hone, J. Shan, and T. F. Heinz. Atomically thin mos_2: A new direct-gap semiconductor. *Physical Review Letters*, 105(13):136805, 2010.

[68] Yan Li, Jun Kang, and Pu Li. Indirect-to-direct band gap transition of the zrs_2 monolayer by strain: first-principles calculations. *RSC Advances*, 4:7396–7401, 2014.

[69] J. He, K. Hummer, and C. Franchini. Stacking effects on the electronic and optical prop-erties of bilayer transition metal dichalcogenides mos_2, $mose_2$, ws_2 and wse_2. *Physical Review B*, 89:075409, 2014.

[70] Liang Li, Lei Shen, and Qibing Pei. Tuning the electronic and optical properties of the zrs_2/pts_2 van der waals heterostructure by an external electric field and vertical strain. *ACS Omega*, 7(43):38464–38471, 2022.

[71] Y. Wang, C. Cong, W. Yang, J. Shang, and T. Yu. Raman spectroscopy study of lattice vibration and crystallographic orientation of monolayer MoS. *Nanoscale*, 7(20):8778–8783, 2015.

[72] Lipin Chen, Zewen Chen, Jinshi Zhao, Laurent Pedesseau, and Charles Cornet. Strain-induced band-to-band fermi level tuning in ii-vi and iii-v antiphase boundaries. *Physical Review B*, 109(8):085404, 2024.

[73] A. Kormanyos, V. Zólyomi, and N. D. Drummond. Tight-binding model and direct band gap of two-dimensional mos_2. *Physical Review B*, 91:195403, 2015.

[74] Y. Liu, W. Ji, and H. Zhang. Strain engineering of two-dimensional materials for elec-tronic and optoelectronic devices. *Nature Nanotechnology*, 12:159–168, 2017.

[75] William Shockley and Hans J Queisser. Detailed balance limit of efficiency of p-n junction solar cells. *Journal of Applied Physics*, 32(3):510–519, 1961.

[76] Zhan Fei, Lu Yang, Lin Yang, and et al. Strain-engineering the electronic structure of transition-metal dichalcogenides. *Nature*, 521:753–756, 2015.

[77] Li He, Shuang Wu, and Xue Duan. Experimental demonstration of a two-dimensional material as a photodetector. *Nature Nanotechnology*, 9:372–378, 2014.

[78] H. J. Conley, B. Wang, J. I. Ziegler, and et al. Band gap engineering of strained monolayer and bilayer mos. *Nano Letters*, 13(8):3626–3630, 2013.

[79] Stefan Grimme, Jens Antony, Stephan Ehrlich, and Helge Krieg. A consistent and accurate ab initio parametrization of density functional dispersion correction (dft-d) for the 94 elements h-pu. *The Journal of Chemical Physics*, 132(15):154104, 2010.

[80] Alexandre Tkatchenko and Matthias Scheffler. Accurate molecular van der waals interactions from ground-state electron density and free-atom reference data. *Physical Review Letters*, 102(7):073005, 2009.

[81] Jiří Klimeš, David R. Bowler, and Angelos Michaelides. Van der waals density functionals applied to solids. *Physical Review B*, 83(19):195131, 2011.
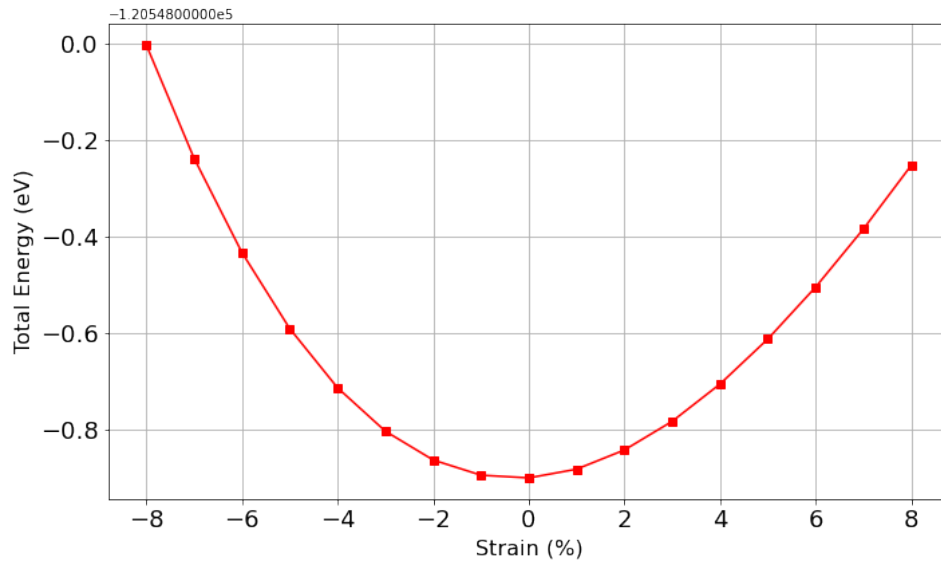
8 Appendix

Figure 23: Total energy of ZrS$_2$ as a function of in-plane strain along the a-b-axis. The curve exhibits a positive parabolic shape with a minimum at 0% strain, indicating that the unstrained configuration corresponds to the system's equilibrium state and lowest energy.

9 Lay summary

Developing new materials with customisable electronic properties is a key area of research in modern science. This dissertation focuses on a material known as ZrS_2, which has exciting potential for use in electronic devices, such as transistors, sensors, and even solar cells. In this project, I explored how ZrS_2's properties can be adjusted by stretching or compressing it in specific directions. This is known as strain engineering and helps us design materials with properties tailored to particular applications, something that is vital for advancing next-generation technologies.

ZrS_2 is part of a class of materials called transition metal dichalcogenides (TMDs). These materials are exciting because their properties can change dramatically depending on how they are treated, which makes them highly versatile. My project focused on understanding how applying strain along the c-axis (the vertical direction) and within the a–b plane (the flat layers) affects ZrS_2's electronic properties. These properties are crucial because they determine how well the material conducts electricity, how easily electrons can move through it, and how it interacts with light, qualities central to most electronic and optoelectronic devices.

ZrS_2 is what scientists call a "two-dimensional" material, meaning it comprises of layers only a few atoms thick, similar to the well-known material graphene. Like graphene, which consists of a single layer of carbon atoms, ZrS_2 can be peeled down to individual atomic sheets. These 2D materials are special because their thin, flat structure makes them highly sensitive to external forces like strain. This makes them easier to engineer than thicker, bulkier materials for specific properties. In the case of ZrS_2, its layered structure means that applying strain along the c-axis (perpendicular to the layers) affects how the layers interact with each other, while straining it in the plane of the layers (a–b plane) affects how atoms within the same sheet behave. This unique behaviour makes ZrS_2 a promising candidate for ultra-thin, flexible electronics.

I used advanced computer simulations based on density functional theory (DFT) to explore this. These simulations solve complex equations to describe how the electrons behave inside the material. By applying different strain levels, both compressive (pushing the material) and tensile (stretching it), I observed how the electronic behaviour of ZrS_2 changes.

The results show that strain dramatically affects the mobility of charge carriers, i.e. how well the material can conduct electricity. When ZrS_2 is compressed along the c-axis, the effective mass of electrons increases, meaning they move more sluggishly, and the material becomes less conductive. In contrast, stretching ZrS_2 along the c-axis reduces the effective mass, allowing electrons to move more freely. This suggests that tensile strain could boost electrical performance in devices that use ZrS_2.

When strain is applied in the a–b plane, the effects are more subtle but still significant. Compression in this direction also increases the effective mass, especially for holes, while tensile strain can slightly reduce it. Overall, the material responds differently depending on the direction and type of strain, which offers a highly desirable control level in materials design.

The key finding from this work is that the effective mass of electrons and holes, an essential factor in determining how easily charge flows through a material, can be finely tuned through strain. By understanding and predicting these changes, we can design material with custom electronic behaviours without altering their chemical composition.

This is important because it opens the door to designing materials with specific electronic characteristics simply by applying mechanical strain. This could lead to more efficient and powerful electronic devices, including low-power transistors, faster computer chips, and more sensitive sensors. Strain engineering could also improve the performance of materials used in renewable energy technologies, such as solar cells, where enhancing the flow of charge carriers is crucial for better efficiency.

In summary, this dissertation explores the fascinating world of materials science by showing how the electronic properties of ZrS_2 can be optimised through strain engineering. The findings provide valuable insights that could lead to the development of more efficient and tailored electronic components with broad applications in computing, sensing, and clean energy. As technology continues to evolve, mastering control over materials at the atomic level will be key to the innovations of tomorrow.